



| | |
|-------------------------------|---|
| Publication Year | 2019 |
| Acceptance in OA @INAF | 2020-12-02T14:23:51Z |
| Title | Close Cassini flybys of Saturn's ring moons Pan, Daphnis, Atlas, Pandora, and Epimetheus |
| Authors | Buratti, B. J.; Thomas, P. C.; Roussos, E.; Howett, C.; Seiß, M.; et al. |
| DOI | 10.1126/science.aat2349 |
| Handle | http://hdl.handle.net/20.500.12386/28628 |
| Journal | SCIENCE |
| Number | 364 |

1 First Results from *Cassini's* Flybys of Saturn's Ring Moons at the End of Mission

2 This paper discusses the preliminary results from 6 Cassini instruments of 5 “closest ever” flybys
3 of Pan, Daphnis, Atlas, Pandora, and Epimetheus to show the surface properties of these moons
4 are determined by two competing processes: accretion of a red chromophore from Saturn's main
5 ring system and of icy particles from Enceladus

6 B. J. Buratti¹, P. C. Thomas², E. Roussos³, C. Howett⁴, M. Seiß⁵, A. R. Hendrix⁶, P. Helfenstein², R. H.
7 Brown⁷, R. N. Clark⁶, T. Denk⁸, G. Filacchione⁹, H. Hoffmann⁵, G. H. Jones¹⁰, N. Khawaja¹², P. Kollmann¹³,
8 N. Krupp³, J. Lunine², T. W. Momary¹, C. Paranicas¹³, F. Postberg¹², M. Sachse⁵, F. Spahn⁵, J. Spencer⁴, R.
9 Srama¹⁴, T. Albin¹⁴, K. H. Baines¹, M. Ciarniello⁹, T. Economou¹⁵, S. Hsu¹⁶, S. Kempf¹⁶, S. M. Krimigis¹³, D.
10 Mitchell¹³, G. Moragas-Klostermeyer¹⁴, P. D. Nicholson², C. C. Porco¹⁷, H. Rosenberg⁸, J. Simolka¹⁴, L. A.
11 Soderblom¹⁸

12 ¹Jet Propulsion Laboratory, California Institute of Technology, Pasadena, CA 91109

13 ²Department of Astronomy, Cornell University, Ithaca, NY 14853

14 ³Max Planck Institute for Solar System Research, 37077 Göttingen, Germany

15 ⁴Southwest Research Institute, Boulder, CO 80302

16 ⁵Department of Physics and Astronomy, University of Potsdam, 14476 Potsdam, Germany

17 ⁶Planetary Sciences Institute, Tucson, AZ 85719

18 ⁷Lunar and Planetary Lab, University of Arizona, Tucson, AZ 85721

19 ⁸Freie Universität Berlin, 12249 Berlin

20 ⁹Istituto di Astrofisica e Planetologia, Via Fosso del Cavaliere 100, Rome, Italy

21 ¹⁰Centre for Planetary Sciences, University College London, Bloomsbury, London WC1E 6BT, UK

22 ¹²Institut für Geowissenschaften, Universität Heidelberg, 69120 Heidelberg, Germany

23 ¹³Applied Physics Laboratory, Johns Hopkins University, Laurel, MD 20723

24 ¹⁴University of Stuttgart, Pfaffenwaldring 29, 70569 Stuttgart, Germany

25 ¹⁵Enrico Fermi Institute, University of Chicago, Chicago, IL, 60637, USA

26 ¹⁶Physics Department, University of Colorado, Boulder, CO 80303, USA

27 ¹⁷Space Sciences Institute, Boulder CO 80301

28 ¹⁸United States Geological Survey, Flagstaff, AZ 86001

36 © 2018. All rights reserved.

37 Submitted to Science Feb. 6 for the Cassini End-of Mission special issue

38 Resubmitted, May 2018

Five “best ever” observations of Saturn’s ring moons Pan, Daphnis, Atlas, Pandora, and Epimetheus were obtained between December 2016 and April 2017 during the Ring-grazing Orbit period of the *Cassini* mission. Unprecedented views of the moons’ morphology, structure, particle environment, and composition were returned, as well as first detections in the ultraviolet and thermal regions of the spectrum. The optical properties of the moons’ surfaces are determined by two competing processes: contamination by a red chromophore in Saturn’s main ring system, and accretion of bright particles from the E-ring originating from Enceladus’s plumes.

Introduction

Saturn possesses a family of small inner irregular moons that occupy dynamical regimes unique to the system. Two moons orbit in gaps within Saturn’s main ring system: Daphnis, which was discovered by the *Cassini* spacecraft in 2005 orbiting in the A-ring’s Keeler gap (1), and Pan, which is found in the Encke gap in the A-ring (2). Three other “shepherd” moons orbit at the edges of the A-ring (Atlas) or the F-ring (Pandora and Prometheus). Finally, the “co-orbital” moons Janus and Epimetheus share horse-shoe orbits outside the F-ring and swap their positions every four years (supplementary materials). Saturn’s rings are almost certainly tied to the origin and continued existence of these moons. The main questions include whether the rings formed from the break-up of an inner moon; if the moons formed from the consolidation of existing rings, either primordial or impact-created; and the identity of key alteration processes acting on the rings now and in the past. The main rings were originally considered unconsolidated primordial debris, unable to form a moon because of tidal forces. Evidence from the two Voyager spacecraft suggested the rings and inner moons were both debris from the breakup of

the same parent body, or perhaps of several parent bodies, with the moons being the largest fragments from the collision (3). *Cassini*'s discovery of low bulk densities for the moons along with dynamical studies and the existence of ridges around the equators of Atlas and Pan suggested the subsequent accretion of main ring particles onto these moons (4-6).

Analysis of the optical properties of the moons including color, albedo, and spectral properties in the visible and infrared between 0.35 and 5.2 μm showed that they resemble the ring systems in which they are embedded or abut (7-10). An elusive low-albedo reddish chromophore that could be organic material, silicates, or nanophase iron (11), and that appears to be abundant in the rings, tinged the moons, a finding that further supported a common origin for them and continuing accretion of particles onto the moons' surfaces. The interactions of the ring system of Saturn with its inner moons may form two distinct zones: an inner region in the vicinity of the main ring system that is dominated by a red chromophore, and an outer region that is dominated by fresh, high albedo icy particles from the E-ring. Complicating the picture, however, is the possible influence of interactions with magnetospheric particles, which were shown to alter the color and albedo of the main moon system of Saturn (12,13). Another key question is whether any volatiles other than water ice exist on the ring moons. Were a molecule with higher volatility than water ice to be found, it would point to material originating in a colder region outside the Saturnian system: the discovery of CO_2 on Phoebe, for example, suggested this outer irregular moon originated in the Kuiper Belt (14).

The last phase of *Cassini*'s mission began on November 30, 2016 and ended on September 15, 2017, with two distinct periods: the "Ring-grazing" (or F-ring) Orbits, when 20 close passes to the F-ring were accomplished, and the Proximal Orbits (the "Grand Finale"), when 23 dives between

the planet and the main ring system were executed. During the Ring-grazing Orbits there were five “best-ever” flybys of Pan, Daphnis, Atlas, Pandora, and Epimetheus. Data were obtained by the four remote sensing instruments on *Cassini*: The Imaging Science Subsystem (ISS; 15); The Visual Infrared Mapping Spectrometer, with medium resolution spectra between 0.35 and 5.1 μm (VIMS; 16); The *Cassini* Infrared Spectrometer (CIRS; 17); The Ultraviolet Imaging Spectrometer (UVIS; 18); and *Cassini*’s fields and particles experiments, two of which obtained simultaneous data that are described in this paper, the Cosmic Dust Analyzer (CDA; 19) and the Magnetosphere Imaging Instrument (MIMI; 20). In this paper we discuss the first results from the closest flybys of these moons, the details of which are summarized in Table 1. In addition to the “closest-ever” flyby of Epimetheus on January 30, 2017, a second flyby of this moon, which was also better than any previous event, occurred on February 21, 2017, with a closest approach of 8088 km. Valuable data on the dust and plasma environment in the vicinity of the small inner moons was also captured by the particles experiments during the subsequent Proximal Orbits.

[Table 1 here]

Geology and morphology

Previous images of the ring moons showed distinctive equatorial ridges on Pan and Atlas (4,5) which were interpreted as likely formed by accretion of ring particles. Images of Daphnis were ambiguous as to the morphology of any near-equatorial ridge. Previous images also showed the small satellites all in synchronous rotation (6), but those at different distances from Saturn had distinctive properties. Prometheus and Pandora’s orbits straddle the F-ring, and although they exhibit different surface morphology, their densities are nearly identical (Table 2). The small (< 5 km mean radius) satellites Aegaeon, Methone, and Pallene that orbit in diffuse rings or ring arcs (21, 22) have smooth ellipsoidal shapes indicative of hydrostatic equilibrium (6). The co-orbital

satellites, Epimetheus and Janus, by far the largest of the inner small moons, were found to have nearly identical mean densities (Table 2), also the highest among the inner small moons. Grooves had been observed on Epimetheus (23), and there were suggestions of discrete crater-filling sediments on both Janus and Epimetheus (6). Epimetheus was observed well enough to establish a ~ 7 deg. forced libration (24).

At the start of the Ring-grazing Orbits, the major puzzles concerning these objects included: Do the differences among the ridges on Pan, Daphnis, and Atlas help constrain their origins and evolution? What structural features are present on these moons, and can they reveal formation or modification history? How is material moved across the surfaces? Are their compositions related to their orbital positions? The six flybys at the end of the *Cassini* mission provided unprecedented spatial resolution and new spectral information on the embedded ring moons to answer some of these questions.

Table 2 provides the best measures of the shapes, volumes, and calculated mean densities of the small satellites of Saturn. The late-orbit image data reduced uncertainties in volume and mean density. Only Epimetheus and Janus have densities significantly above 500 kg m^{-3} ; the lowest possible mean densities of ring satellites are below 300 kg m^{-3} . Surface accelerations vary substantially across each object due to shapes and especially tidal accelerations (Table 2).

[Table 2 here]

Main Ring moons and ridges

The high resolution data make clear that the equatorial ridges on Pan and Atlas are distinct from what appears to be a more structurally competent “core” of each moon, and that ridges are different

on all three main ring satellites. The fractional volumes of the ridges are Pan ~10%; Daphnis ~1%, and Atlas ~25%. Atlas's ridge is smooth at 76 m/pixel, with some elongate to irregular brighter albedo markings. It grades into a core with distinct ridge and groove topography (Fig. 1.), with a slightly polygonal equatorial profile previously known (6). Pan's ridge has distinct topographic margins with the core, with a somewhat polygonal equatorial shape, and it has some grooves, small ridges, and even some small impact craters. Meridian profiles across Pan's ridge vary considerably with longitude. Fig. 2 shows Pan in the best northern view, with calculated relative gravitational topography and surface slopes. Pan's ridge is not the result of material sliding toward areas made low by rotation and tides as are some ridges on small asteroids (27, 28) as slope directions are not latitudinally directed. The distinct boundary between ridge and core, the distinct surface morphology on each, and the large differences in relative heights along the ridge require the formation of this ridge to be unrelated to surface, gravity-driven processes. These observations are consistent with formation of the ridge by accretion of particles, the pattern being dictated by the relative orbital and rotational dynamics of the core and ring particles (4).

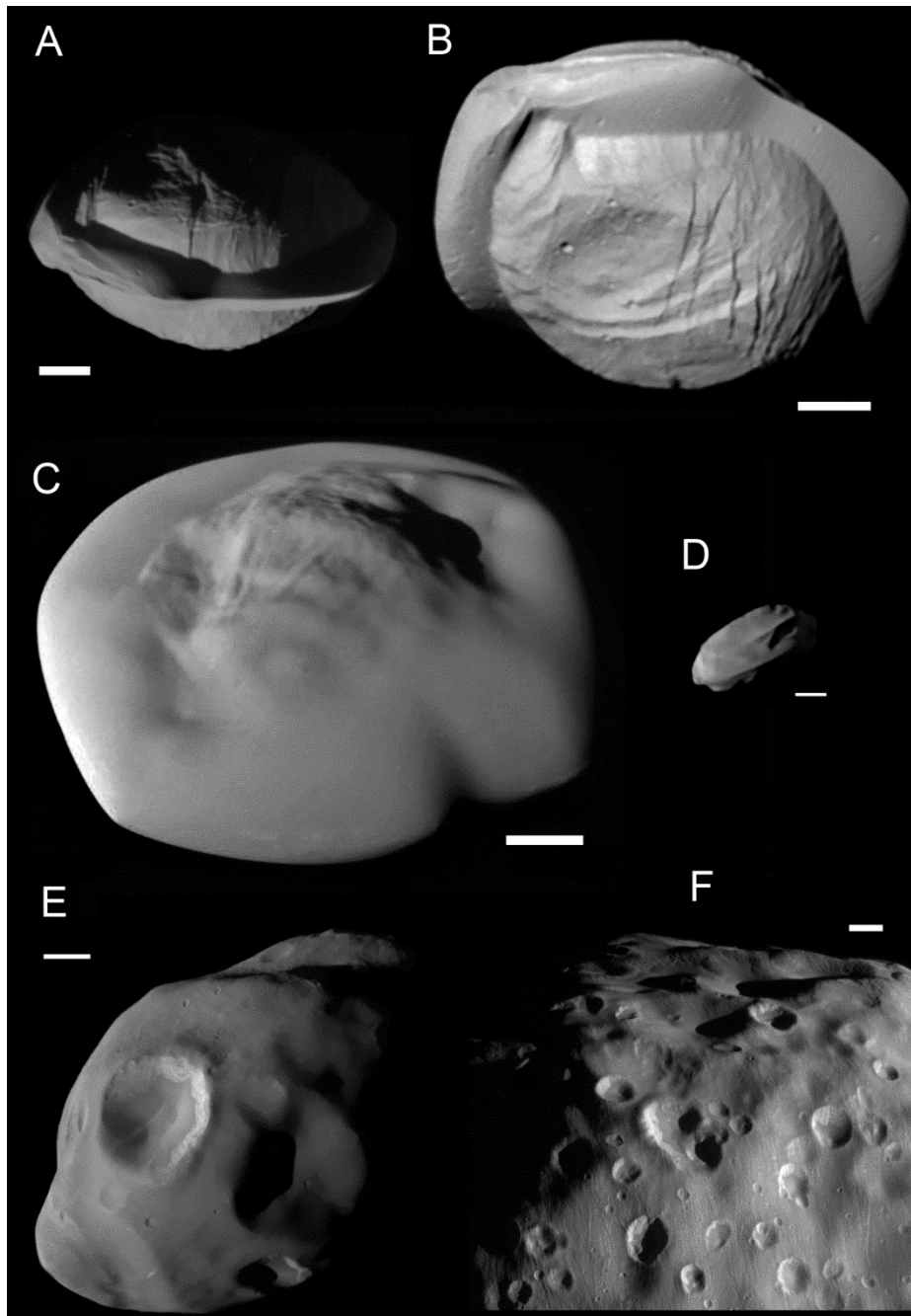


Fig 1. **Ring moons.** (A) Pan, N1867606181, from 26°S. Scale bar 5 km. Obtained at 182 m/pixel
 (m/p). (B) Pan, N186704669, from 39°N; scale bar 5 km; 147 m/p. (C) Atlas, N1870699087, from
 40°N; scale 5 km; anti-Saturn point at lower left; 108 m/p. (D) Daphnis, N1863267232, from 14°N;
 anti-Saturn point to left; scale 2 km; 170 m/p. (E) Pandora N1860790629 Scale bar 10 km. Sub
 spacecraft point is 35°N,98°W; north pole is close to two small craters above large, bright-walled

crater; 240 m/p. (F) Epimetheus. N1866365809; Grooves and craters dominate the surface. Scale 5km; 99 m/p. (The N numbers are the image identifiers.)

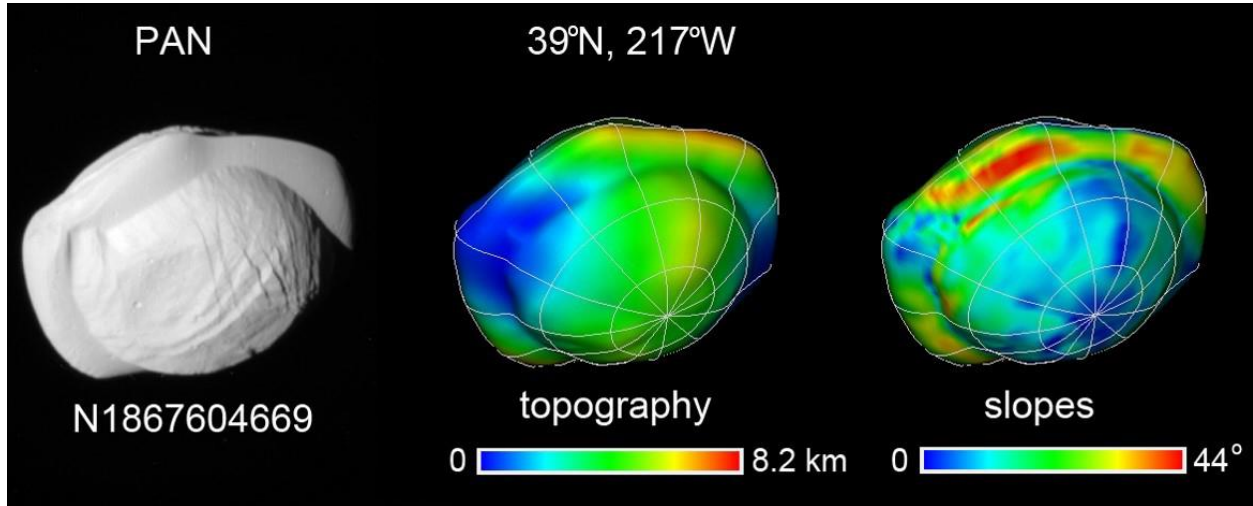


Fig. 2. Relative topography and slopes on Pan. Topography is relative potential energy at surface due to assumed homogeneous interior density, rotation, and tides, divided by an average surface acceleration. Slopes are angles between surface normals and net acceleration vectors (negative).

The nominal mean densities of all three main ring moons give calculated surface accelerations near zero at the sub- and anti-Saturn points. The remainder of all the surfaces has inward directed net accelerations. These results suggest the ends may be limited by their ability to accrete materials, but there is much to be explored in the dynamics of accreting and/or modifying these ridges.

The surfaces of the ring moons may be crudely divided into three units on the basis of morphology, geography, and texture of surface visible at the available resolutions (Fig. 3). The equatorial ridges generally have smoother surfaces than do the “cores.”

The cores have more impact craters than do the ridges on Pan and Atlas which display a few sub-kilometer impact craters. Pan and Atlas’ cores show lineated topography indicative of body structure. Pan has two distinct global sets of quasi-parallel faults, one of which is roughly concentric to the long axis and exhibits conspicuous scarps and terracing from likely equatorward displacements. Axial symmetry of this system suggests that tidal forces were involved in its development. The second system trend is oblique to the first, and is well expressed in both north and south hemispheres (Figs.1, 3). By contrast, Atlas’ core exhibits patterns of elongated ridge and groove topography that do not have fault scarp morphology, and appear covered by at least tens of m of loose regolith.

Pan’s equatorial ridge is thickest north-south at longitudes of approximately 220°, 310°, 135°, and 50° W, yet its radial extent peaks at longitudes of 5°, 55°, 100°, 180°, 235°, and 310°. It supports grooves and small craters: their presence suggests some cohesion in this extreme low-g environment. Atlas’s equatorial profile is also somewhat polygonal, but not as pronounced as Pan’s.

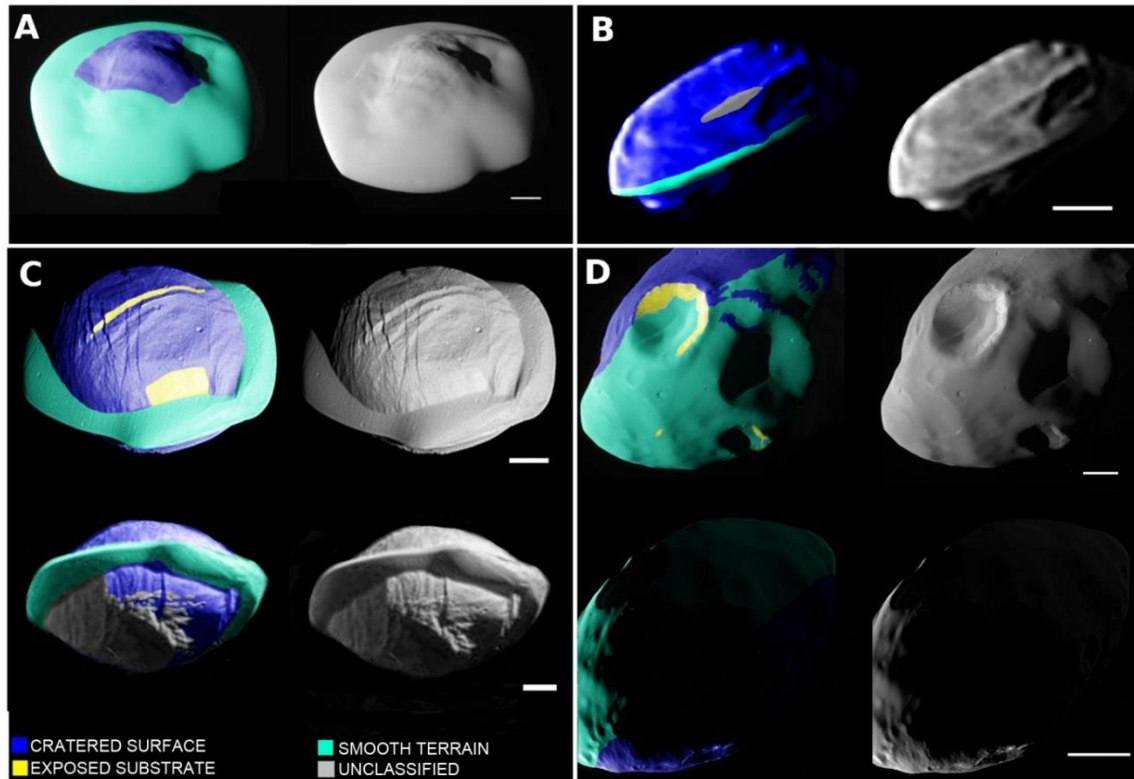


Fig. 3. Distribution of three primary units on ring moons (A) Atlas, scale bar 5 km. Obtained at 94m/pixel (m/p). (B) Daphnis, scale bar 2km; 167 m/p. (C) Pan scale bars 5 km; 144 m/p (top) and 279 m/p (bottom). (D) Pandora (top scalebar, 10km, bottom, 20 km); 137 m/p (top), 200 m/p (bottom). Cratered surface: heavy cratering, relatively crisp surface relief, and regolith typical of other small bodies in the Saturnian system. Smooth terrain: distinctly smooth compared to typical small body cratered surfaces; some is material collected in crater floors. Exposed substrate: relatively bright with lineations more typical of rigid materials than of loose regolith. Unclassified materials are those for which insufficient data are available to resolve ambiguities between terrain types.

The classification of some material units on Pan's southern hemisphere is ambiguous, in part because more of these regions are illuminated only by Saturnshine. These currently unclassified

units in Fig. 3 include knobby streaks of hummocky material that trend approximately parallel to the equator and hummocky deposits that outline a curvilinear depression on the Saturn-facing side.

The best-available spatial resolution of Daphnis imaging is poorer, 170 m/pixel vs. that of Pan (147 m/pixel) and Atlas (76 m/pixel), and Daphnis is only about a quarter the dimensions of the other ring moons. As a result, it is not clear that its near-equatorial ridge is any smoother or otherwise different from the rest of the satellite surface. The equatorial ridge extends at least from 75°W to 185°W. An additional ridge at 22°N runs from ~ 60°W to 120°W. Both ridges are 300-400m north-south, and perhaps radially 300 m in extent. The core has an elongated (2.5 km) depression that is roughly aligned east-west.

F-ring moons

Prometheus and Pandora orbit inside and outside the F-ring. The higher resolution achieved on the Pandora flyby provided better coverage of the geography of grooves and debris on the surface of this “shepherding” moon (Fig. 1). Although many of the grooves form a familiar pattern concentric to the major axis of the body, there is a slight offset of the pattern especially noticeable on the sub-Saturn side, which reflects the orientations mapped earlier (21).

ISS closeup images of Pandora revealed that part of the leading hemisphere seen in Fig. 1 is smooth in comparison to other regions of Pandora (Figs. 1,3). The smooth deposits are most continuous near the equator but they become patchy at high latitudes where they appear to be too thin to mute the coarse surface relief along protruding crater rims. The smooth deposits extend approximately $\pm 60^\circ$ in latitude, most like the broad extent of the ridge on Atlas. This arrangement might indicate

the accretion of material as on the main ring moons. If so, its efficacy on Pandora is at least two orders of magnitude smaller than on Pan and Atlas, and much broader latitudinally. However, variations in resolution, illumination, and viewing geometry make mapping of textural variations on Pandora ambiguous.

Co-orbitals

The highest resolution images of the flybys were of Epimetheus, the smaller of the co-orbitals, reaching scales of 36 and 49 m/pixel. These data greatly enhanced mapping of grooves and sediment coverings, both seen in lower resolution data (23). The grooves are global in occurrence, and are largely the typical beaded to straight, elongated depressions that appear to be features formed in loose regolith. There are some exposures of brighter material apparently devoid of regolith cover (Fig. 1F) that also show elongate lineations, generally slight depressions. These align with the grooves nearby that appear to be regolith features, and largely align with the regolith groove global patterns. This association appears to support a relation of at least some regolith grooves to fractures or other structures in a more rigid underlying “bedrock,” although the variety of groove morphologies on many objects suggest grooves may have a multiplicity of origins (29, 30, 23, 31). The highest resolution images also show exposures of crisscrossing linear ridges and other lineations. If representative of the interior, these features suggest structure and history far different from simple accumulation of a “rubble pile.”

Colors of the Small Ring Satellites and Pandora

The whole-disk colors of the ring satellites as measured in ISS broadband filters (32) follow similar trends with distance from Saturn as those found by the VIMS instrument (7-10). The ISS Narrow

247 Angle Camera (NAC) uses paired broadband filters. The CL1:UV3 pair (341 nm) and CL1:IR3
 248 pair (930 nm) span the spectral range of the camera, and IR3/UV3 ratios can represent the ratio
 249 of observed brightness values in each of the broadband filters (cf. 6). For reference, Enceladus,
 250 the presumed source of ice particles that mute colors on other satellites, has an effectively neutral
 251 IR3/UV3 ratio of 1.03 ± 0.02 (33).
 252
 253 Pan, Daphnis, and Atlas are expected to show effects of material deposited from the rings. Closest
 254 to Saturn, Pan's average IR3/UV3 ratio of 2.5 ± 0.2 is red but significantly smaller than the value
 255 of 3.3 ± 0.2 of the adjacent A-ring (i.e., it is less red than the rings). Further out, the A-ring
 256 IR3/UV3 ratio decreases from 2.7 ± 0.2 on the inside of the Keeler gap (which contains Daphnis)
 257 to 2.2 ± 0.3 on the outside. The mean value is not statistically different from the value of 2.3 ± 0.3
 258 of Daphnis itself. The equatorial ridges on the ring satellites may be very old (4) but the colors
 259 most likely reflect a patina of material deposited from geologically recent and ongoing processes.
 260 Atlas, which falls just outside the A-ring has an IR3/UV3 ratio 2.4 ± 0.1 . Pandora, with its value
 261 of 1.9 ± 0.1 , is close to the F-ring further from Saturn. It lacks an equatorial ridge but possesses
 262 smooth deposits which on the leading side extend from the equator to mid-latitudes.
 263 Among the terrains shown in Fig. 3 color differences can be identified from the high-resolution
 264 images on all but Daphnis, for which the CL1:UV3 images were badly blurred by spacecraft
 265 motion. The IR3/UV3 ratio for cratered materials on Pan is about 19% higher than for its equatorial
 266 ridge and is most like the average global value. Similarly, the ratio for cratered materials on Atlas
 267 is about 16% higher than for its ridge, but in this case, the global average value not surprisingly
 268 most closely matches that for Atlas' larger equatorial ridge. For Pandora, the cratered materials
 269 have a IR3/UV3 ratio that is 15% *lower* than for the smooth materials towards the equator. The

global average ratio is in between that for the cratered material and the smooth deposits. Exposed substrate is visible as a scarp on Pan and a bright exposed crater wall on Pandora. On Pan, the IR3/UV3 ratio of exposed substrate is intermediate between the ridge materials and crater materials. However, on Pandora, the corresponding ratio for the exposed crater wall is not statistically distinguishable from that of the cratered material.

Composition

Most of the compositional information on the surfaces of Saturn's moons has been obtained by VIMS (16).

Prior to the close flybys of the ring moons, some spectra were gathered by VIMS and rudimentary compositional information was obtained (7-10). Water ice was the only volatile identified, but the moons' visible colors varied, especially in the 0.35-0.55 μm spectral region, which suggested contamination by a reddish chromophore that perhaps came from the ring system itself. The identity and source of this chromophore was one of the main questions still remaining at the final stages of the *Cassini* mission. (This coloring agent is distinct from the low-albedo red material from the Phoebe ring that is deposited on the leading hemisphere of Iapetus and on Hyperion (7, 8).)

The close flybys of the embedded moons Daphnis and Pan enabled the acquisition of spectra of these moons for the first time, although only an IR spectrum (1.0-5.0 μm) for Daphnis was successfully obtained. These new data provide a key test for the origin of the red chromophore in the inner Saturnian system. These observations also provide rudimentary information on spatial variations in composition on the moon's surfaces, although the resolution is only about 1-2% (depending on the instrument mode) of ISS's (supplementary materials)

Fig. 4 shows the spectrum of each moon from 0.35-5.0 μm (1-5.0 μm for Daphnis). The only spectral absorption bands detectable in these images are the water ice bands at 1.25, 1.6, 2.0 and 3.0 μm . No other volatiles are detectable, including CO_2 , although its prime absorption band in this spectral region is at 4.26 μm , which is in the noisy region of the spectrum beyond about 3.5 μm . One interesting feature of these spectra is the relatively large depth of the absorption band for crystalline water ice at 1.65 μm . This spectral band is sensitive to radiation damage (34); its unusual depth implies a lack of this type of damage in the ring environment, which is expected given the dearth of high-energy particles in the rings (see the section on particle observations). Water ice spectral bands are also sensitive to grain size, with deeper bands signifying larger sizes (35). A larger particle size could signify larger regolith grains in the main ring system than in the E-ring, or it could simply be due to gravitational escape of the smaller particles, some of which could be formed by continual impacts.

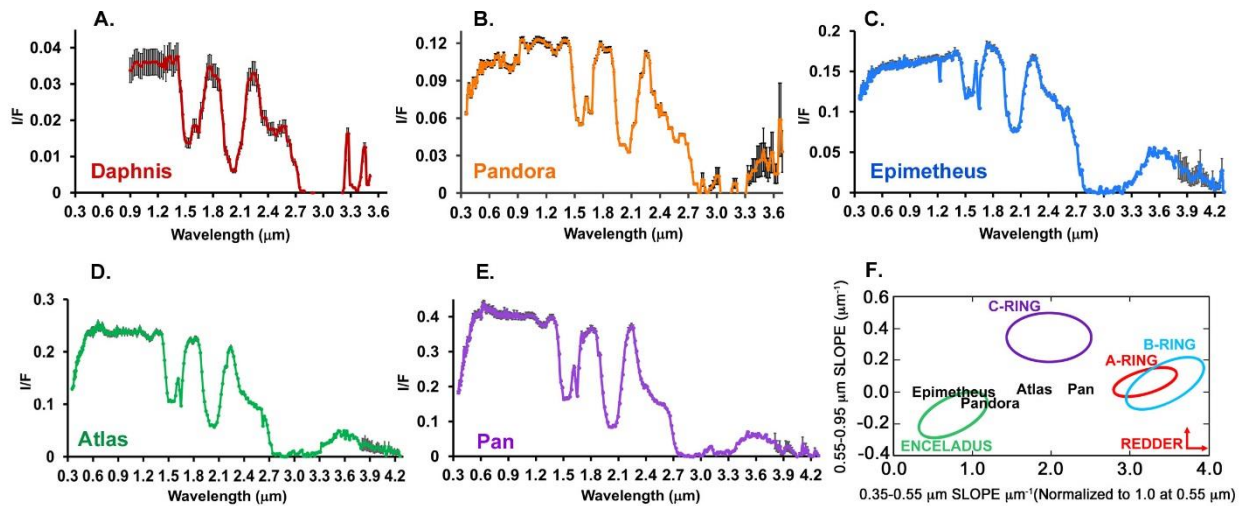


Fig. 4A-E. Spectra of the five moons from 0.35-5.1 μm . 5F The colors of Saturn's main ring system and Enceladus (7,8) compared with those of Epimetheus, Atlas, Pandora, and Pan. There is a gradient depending on the position of the moon with respect to the rings, with Pan,

309 which is embedded in the Encke gap, being the reddest and Epimetheus, which is farthest from the
310 rings and closest to Enceladus, being the bluest. This effect results from the countervailing
311 processes of contamination by a red chromophore from the main rings and ice particles from the
312 E-ring, which is formed from particles from Enceladus.

313 The VIMS visible colors show good agreement with those derived by ISS with equivalent VIMS
314 numbers of the IR3/UV3 ratios of 2.7 ± 0.3 for Pan; 2.2 ± 0.2 for Atlas, 1.7 ± 0.2 for Pandora, and
315 1.5 ± 0.1 for Epimetheus (the VIMS spectrum extends to only $0.35 \mu\text{m}$: this value was used for
316 UV3 and the error bars adjusted accordingly). The moons embedded in the rings show important
317 spectral differences with the surrounding rings; in general they are less red (Fig. 5F). The VIMS
318 ratio image of Atlas shows uniformity between the main body and its equatorial ridge, at least in
319 water ice abundance, which implies accumulation of particles away from the equator to provide a
320 globally homogeneous surface. Color differences below the spatial resolution of VIMS may exist,
321 as detected by ISS in the visible.

322 The most striking difference among these new spectra is the difference in color measured by the
323 slope between 0.35 and $0.55 \mu\text{m}$. The new spectrum of Pan is extraordinarily red compared to
324 other Saturnian moons. Atlas, the shepherd moon just outside the A-ring, is also red but less so,
325 and Pandora, which is associated with the F-ring, even less. The color of Epimetheus is more like
326 that of the medium-sized moons (7-9). Thus, there is a gradient in color with distance from Saturn's
327 ring system, with the embedded Pan being the most red. This view is clear in Figure 5A-E, where
328 the slope of the visible spectrum increases sharply as the distance to Saturn increases, and it is
329 quantified in Fig. 5F, which shows the visible colors derived from the recent close flybys with the
330 colors of the main ring system of Saturn (8). These results imply the red chromophore comes from
331 the rings themselves. However, the differences in color between the moons and their adjacent rings

– the small moons are consistently bluer than their surrounding rings - could be due to another contaminant: particles of almost pure water ice from the E-ring. This ring is a diffuse torus that is fed from the plume of Enceladus. The particles have a wide range of orbital elements and predominately impact the leading sides of the main moons (or the trailing side of Mimas) to alter their albedo and color (36-38). The ring moons’ leading hemispheres would tend to be “painted” by fresh grains and accrete more water ice than the surrounding ring particles.

The depth of the water ice band at $2.0\ \mu\text{m}$ compared to the continuum at $1.8\ \mu\text{m}$ ($1.8/2.0\ \mu\text{m}$) is 5.2 ± 0.1 for Pan, 5.0 ± 0.2 for Daphnis; 4.4 ± 0.1 for Atlas, 3.4 ± 0.1 for Pandora, and 2.4 ± 0.1 for Epimetheus. The band-depths increase closer to Saturn, most likely due to the increasing particle sizes (35). This view is consistent with the moons embedded in the ring (Pan and Daphnis) being coated with main ring particles rather than with smaller particles from the E-ring. (The absorption band at $1.6\ \mu\text{m}$ shows a similar but weaker trend).

Interactions between moons and magnetospheric particles can also alter the moons’ colors and albedos (12, 13). However, results from the fields and particles experiments in the vicinity of these moons showed a dearth of high energy particles with the expectation that these alterations would be slight (see below).

First Ultraviolet and Thermal Infrared Detections of the Small Moons of Saturn

During the Ring-grazing Orbits the spacecraft was in a radiation and dust environment that resulted in high background levels for UVIS. One successful detection was made of Epimetheus during the encounter on Feb 21, 2017. Even on that flyby, the signal is only above the background for the longest FUV wavelengths, $\sim 0.170\text{-}0.19\ \mu\text{m}$. However, this single UV measurement of reflectance

places some constraints on surface composition and exogenic effects on Epimetheus. At 72° solar phase angle (the angle between the spacecraft, Epimetheus, and the Sun), the derived normal reflectance averaged between $0.17\text{-}0.19\ \mu\text{m}$ is 0.09 ± 0.02 . For comparison, this number is roughly 1.5-2 times lower than the reflectance measured at Tethys under similar viewing geometry; however, Tethys has a significantly higher visible geometric albedo (~ 1.2 compared to ~ 0.73 for Epimetheus (36)), which indicates that Epimetheus may have a roughly uniformly lower reflectance than Tethys in the UV-visible range. The UV-visible spectral slope and albedo are strongly driven by exogenic effects, since this spectral range senses the uppermost layer of the regolith affected by processes including radiolysis and E-ring grain bombardment. The UVIS result combined with the knowledge of the visible albedo may suggest that Epimetheus is not as affected by the brightening effects of the E-ring grains as Tethys is (36), or that there is some other darkening agent or process important at Epimetheus's location. Thus, the UV-visible albedo of Epimetheus may simply reflect the relative importance of the alteration by the reddish lower-albedo chromophore and the icy E-ring particles at this moon's distance.

CIRS made positive detections of two moons: Epimetheus and Atlas (supplemental materials). The results are given in Fig. 5, which shows the temperature that has a blackbody emission curve best able to fit the observed radiance over all wavelengths. Both Epimetheus and Atlas are clearly visible above the background dark sky. The mean surface temperature observed on Epimetheus is $90.1\pm2.7\ \text{K}$, and $82.4\pm4.7\ \text{K}$ on Atlas.

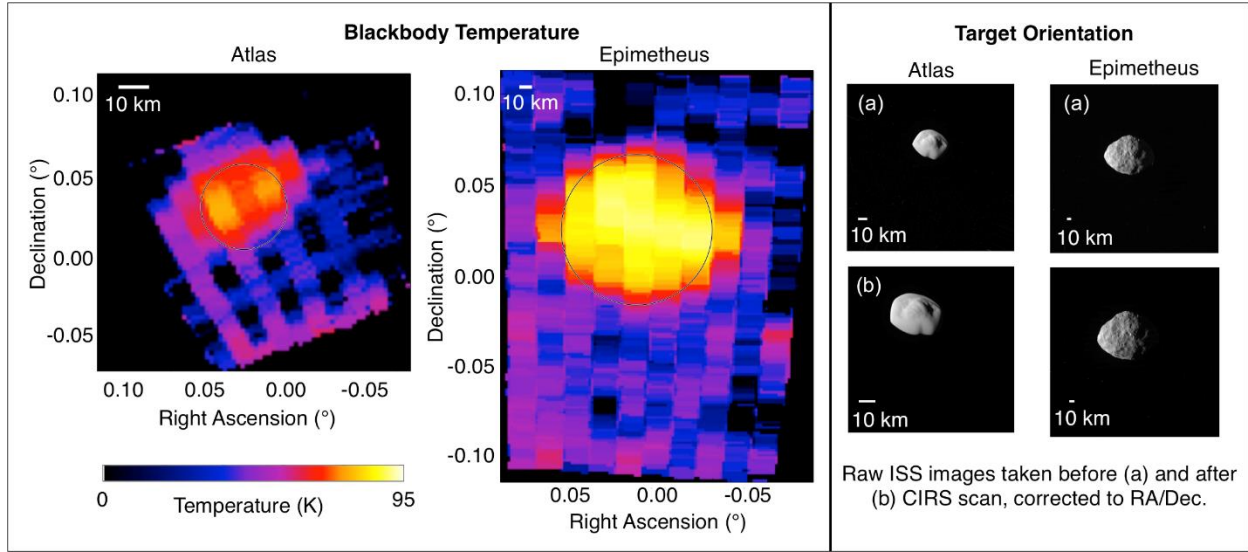


Fig. 5. CIRS and ISS observations of Atlas and Epimetheus. Left: The blackbody temperature of the two targets, as determined by fitting a blackbody curve to the full CIRS radiance spectrum at each location. The results are shown in Right Ascension/Declination space, which has been corrected so the center of the target lies at $0^\circ/0^\circ$. Right: Raw ISS observations of both targets taken before and after the CIRS scan (supplemental materials).

Particle Observations

Throughout the Ring-grazing Orbits, the Particle and Fields experiments obtained unprecedented coverage of Saturn's plasma and dust environment, including detailed measurements of the region around the small inner moons. First results from the analysis of this data provide a basic understanding of whether the surfaces of these bodies are altered by the dusty plasma, and what effects the moons have on the environment, such as forming tori or cavities.

In the course of the Ring-grazing Orbits, *Cassini* passed close to the orbits of the co-orbital moons Janus and Epimetheus. During 11 of the 20 ring plane crossings, the High Rate Detector (HRD) of CDA detected in total about 2,000 dust grains with radii larger than $0.8 \mu\text{m}$. While the vertically integrated number density of grains smaller than $1.6 \mu\text{m}$ does not depend on the radial distance to

Saturn, the density of bigger grains drops by about 50% over a radial distance of approximately
 3500 km (Fig. 7). The larger particles are less susceptible to non-gravitational forces and, therefore,
 particles ejected from the moons stay closer to their parent bodies and form a more confined ring
 (39). The fit of a Gaussian distribution including the dust background from the F- and G-rings to
 the HRD data constrains the radial width of the ring (FWHM) to about 4,300 km leading to a total
 number of ring particles larger than $1.6 \mu\text{m}$ of $2 \cdot 10^{19}$.

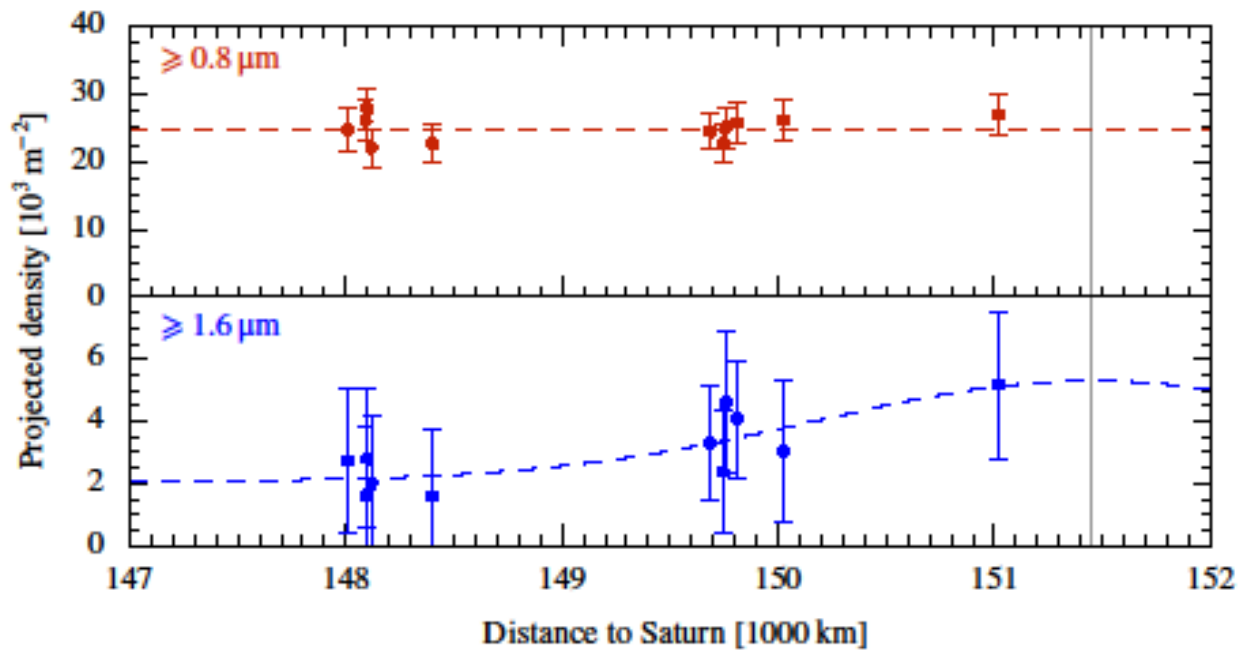


Fig. 7. **Radial density distribution obtained from *Cassini* CDA-HRD dust measurements.**
 While the density of the $> 0.8 \mu\text{m}$ sized particles can be well-fitted by a constant profile (red dashed
 line), the density of the $\geq 1.6 \mu\text{m}$ sized particles decreases inward from the orbit of Janus and
 Epimetheus. The dust distribution of the larger particles is modeled by a Gaussian distribution
 (blue dashed line) with a maximum at the mean radial position of Janus and Epimetheus (vertical
 gray line) including a constant background density.

Many dust rings are formed by ejecta from high-velocity impacts of interplanetary micro-meteoroids eroding the surfaces of satellites without atmospheres. The measured particle number in the Janus-Epimetheus ring constrains the poorly known parameters of the impact-ejection dust creation model (40,41) at Saturn, although more recent work by CDA indicates a higher flux. Using an unfocussed flux of $> 2.7 \cdot 10^{-16} \text{ kg m}^{-2} \text{ s}^{-1}$ with an impact speed of 4.3 km s^{-1} (42), the dust production rate from both moons is about 0.91 kg s^{-1} . (0.64 kg s^{-1} from Janus and 0.27 kg s^{-1} from Epimetheus). This corresponds to $9.8 \cdot 10^{11}$ particles larger than $1.6 \mu\text{m}$ per second ($6.9 \cdot 10^{11} \text{ s}^{-1}$ from Janus and $2.9 \cdot 10^{11} \text{ s}^{-1}$ from Epimetheus) assuming a cumulative power law size distribution $\propto s^{-\alpha}$ with $\alpha = 2.4$ and a maximal ejecta mass of $1 \cdot 10^{-8} \text{ kg}$ consistent with observations of impact-generated dust clouds around the Galilean moons (43, 40).

To explain the measured number of ring particles, this comparably high production rate requires a shallow slope of the cumulative ejecta velocity distribution $\propto v^{-\gamma}$ ($\gamma=1$), and a higher kinetic energy dissipation than predicted by laboratory experiments (kinetic energy ratio of ejecta to impactor is 5%). This points to a highly dissipative and porous (snow or regolith) surface. With this result, we find that most impact-ejecta are gravitationally bound to the moons and fall back to their surface, while only about 6% of them escape to the ring. Numerical simulations reveal that most of the ring particles are recaptured by Janus and Epimetheus after an average lifetime of 60 years resulting in an estimate of $1 \cdot 10^{20}$ ring particles larger than $1.6 \mu\text{m}$. This is, considering the large uncertainties of the impact-ejection model, in fair agreement with the observed value of $2 \cdot 10^{19}$.

Additionally, the CDA Chemical Analyzer (8) has recorded spectra of submicrometer-sized dust particles ($0.1 \mu\text{m} - 0.4 \mu\text{m}$). The compositional analysis of these spectra shows mostly ice grains

but also a few percent pure silicate grains or ice-silicate mixtures. The source of the icy particles could either be the inner edge of the E-ring or surface ejecta of the nearby small ice moons. Because silicate-rich grains of this size have not been detected in the E-ring, these must originate from a different source, possibly the nearby moons Janus and Epimetheus or the F- and G-rings.

The Low Energy Magnetospheric Measurements System (LEMMS) of the MIMI energetic charged particle detector made the first comprehensive survey of the planet's radiation belts inward of Saturn's G-ring and monitored the environment of the five small moons. LEMMS measures energetic electrons and ions from 18 and 27 keV respectively, and well into the MeV energy range. The region inward of Saturn's G-ring has been sampled in the past on several occasions with Pioneer 11 and *Cassini* (44-46). It contains the location where both proton and electron radiation belts have their highest intensities, between the G-ring and Janus and Epimetheus's orbits. Inward of that maximum intensities drop gradually up to the outer edge of Saturn's A-ring which absorbs all energetic particles. Superimposed on the radial profile of radiation belt fluxes are localized dropouts originating from Saturn's moons and rings (47). While several of these features can be attributed to specific moons, like Janus and Epimetheus (48), any influences by Pandora, Prometheus and Atlas (orbiting within the radiation belt boundaries) are less clear. These moons orbit close to Saturn's A and F-rings and separating the different contributions was not possible until now due to the low statistical significance of any past observations. Understanding how effectively these moons sweep-out particle radiation is also important for describing the space weathering environment to which their surfaces are exposed to.

Fig. 8A shows count-rates of >12 and >25 MeV protons as a function of L-shell (L), averaged from all the Proximal Orbits. The L-shell is defined as the distance from Saturn that a field line intersects the magnetic equator and is given in multiples of the planet's radius (1 R_s = 60268 km). The L-shell here describes the equatorial footpoint of Cassini's trajectory mapped along Saturn's magnetic field, normalized to one planetary radius of 60268 km. A third-order multipole model for Saturn's internal magnetic field was used to derive its value (47). The plot shows the well-established sectorization of the MeV proton radiation belts, due to the moons and rings that absorb any protons diffusing across their orbits (50,51). Among these different sectors, the least characterized is the one we mark here as the "Minor Belt", centered at approximately $L=2.29$ and sampled only twice before the Proximal Orbits. The belt gap outward of the Minor Belt is centered near the F-ring ($L\sim 2.32$) and the increased sampling of that region has verified that those gap's boundaries coincide with the L-shells of Prometheus and Pandora (Fig. 8A - inset). Pandora and Prometheus are therefore absorbing protons at a rate that is strong enough to counter the diffusive influx of protons from the surrounding belt sectors. Effectively, the two moons and the F-ring form an extended obstacle to proton radiation. The net result is that the weathering of Pandora's and Prometheus's surfaces by energetic protons is negligible since they orbit within the proton radiation gaps they create. Atlas's effects could not be distinguished from those of the A-ring, but that moon is also exposed to very low proton fluxes. Overall, it is now established that almost all of Saturn's inner moons (except Dione, Rhea or minor moons like Anthe or Pallene) orbit in energetic ion free environments (52-54), a striking difference from that of the Jovian satellites whose surface chemistry and exospheric properties are strongly affected by irradiation from high fluxes of keV and MeV protons, oxygen and sulfur (55,56).

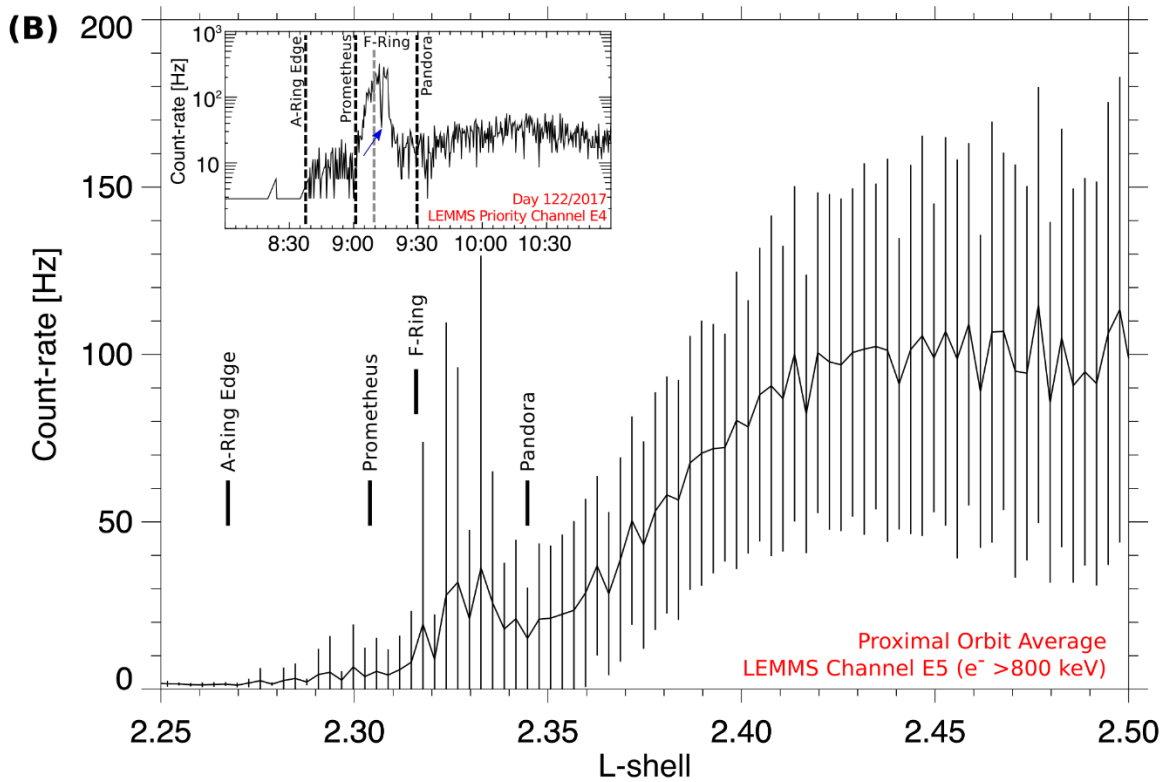
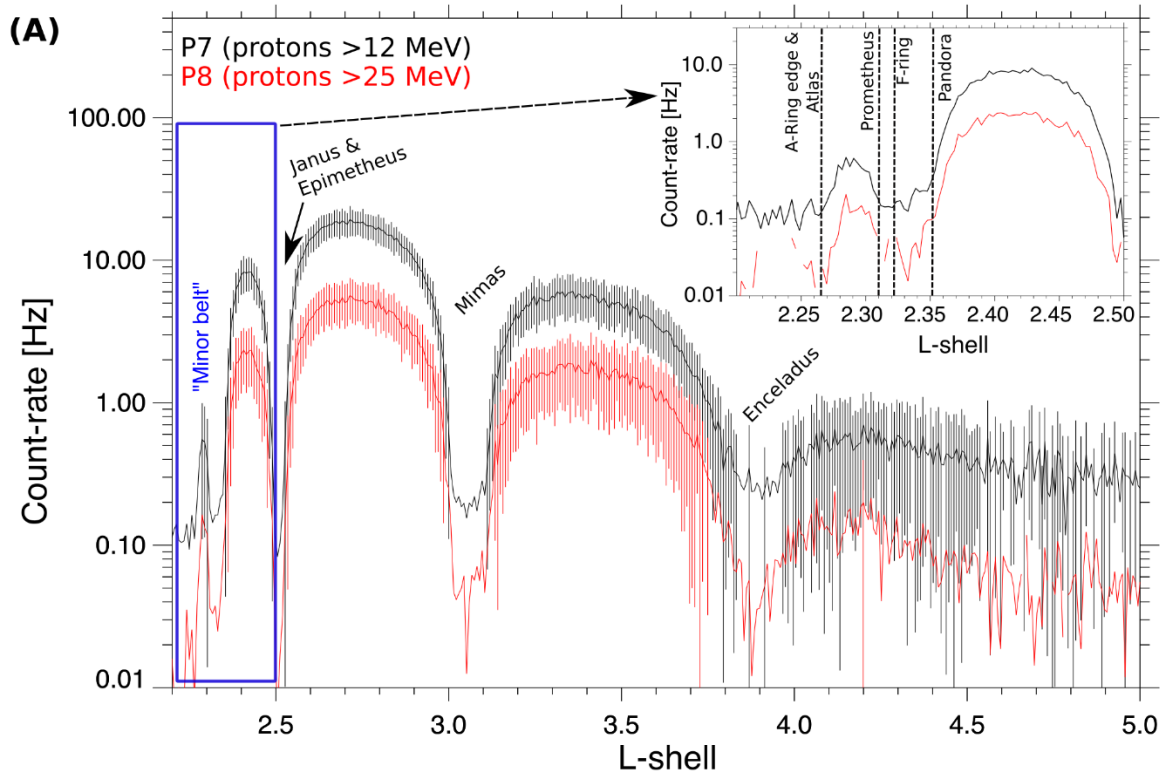


Fig. 8A. **Proximal orbit averaged count-rates of MIMI/LEMMS proton channels P7 and P8 (above 12 and 25 MeV respectively) as a function of L-shell, together with the 1- σ error bars.**

Absence of error bars indicates an error larger than the corresponding mean value. The orbits of several of Saturn's large icy moons are also marked. The inset zooms into the region of the Minor Belt, highlighting the absorbing effects of Atlas, Pandora, Prometheus and the A- and F-rings. Fig. 8B. **Proximal Orbit averaged count-rates of MIMI/LEMMS electron channel E5 (>800 keV)**

as a function of L-shell. Overplotted are the 1- σ error bars at each L-shell bin. The locations of various moons and rings are also marked, as in Panel A. The inset shows time series of high time resolution observations (1 sample per 0.3125 sec) from LEMMS channel E4, which has a similar response to E5. The data were obtained from the second proximal orbit, on May 2, 2017. A blue arrow marks an electron microsignature within one of the MeV electron "spikes" seen consistently during *Cassini*'s outbound crossings near the L-shell of the A-ring's outer edge.

Fig. 8B shows Proximal Orbit averages of electron count-rates from LEMMS channel E5 (>0.8 MeV) as a function of L-shell. Electron radiation levels are more variable than those of protons, as the sizeable error bars indicate, since moons and rings are not effective in sweeping out electrons from their orbits (47,52,57). Inside L=2.4 (inwards of the Janus and Epimetheus orbits) electron rates start to experience a shallow drop towards the outer edge of the A-ring (L=2.27). This drop is interrupted by an unexpected enhancement of the mean electron rates, near the L-shells of the F-ring, Pandora and Prometheus. The statistical 1- σ error bars in that location span more than two orders of magnitude in amplitude, indicating also much higher variability than in the surrounding regions. A survey of electron measurements from each Proximal Orbit reveals that this large scatter is attributed to spiky enhancements of MeV electron fluxes observed in all the outbound crossings

outwards of the A-ring's edge and between $L=2.31$ and $L=2.35$. The radial extent of an individual spike is less than 1800 km along the equatorial plane, and the electron intensity within them can be enhanced by as much as a factor of 300 compared their surroundings. The inset of Fig. 8B shows one such resolved spike, captured by the high time resolution measurements of LEMMS Priority channel E4 (0.8-4.2 MeV) on May 2, 2017. Since measurements in the inbound portion of *Cassini*'s orbit showed no evidence of similar spikes in the same L-shell range, we deduce that these features are fixed around local noon, and their longitudinal extent ranges between 22° and 37° starting from a magnetospheric local time of 14:50 and in the clockwise direction. The longitudinal extend cannot be constrained in the anticlockwise direction. Most of these enhancements were seen around the L-shells of the F-ring, Prometheus and Pandora. This unexpected electron belt component is therefore limited in local-time range. As a result, energetic electron bombardment of the three moons is variable in intensity, episodic and will occur only for a fraction of their orbit around Saturn. Material interaction signatures of energetic electrons are seen as localized depletions (microsignatures) within the electron spikes. These may have come from Atlas, Prometheus, Pandora or F-ring clumps (58); an example is shown with a blue arrow in the Inset of Fig. 8B and could have formed only after the electron enhancement developed. The age of such microsignatures can therefore set limits to the lifetime of these transient electron structures and inform theories of their formation.

Finally, a first survey of the LEMMS measurements from times that *Cassini* was magnetically connected to Saturn's main rings shows no discernible signal of trapped electron or proton radiation above the detection limit of the instrument at the orbits of the Keeler and Encke gaps, where Daphnis and Pan are orbiting.

517

518 **Summary and Conclusions**

519 The low densities of the small moons of Saturn, which were refined by these close flybys, are
520 consistent with accretion from ring material. The new data on the moons embedded in the A-ring
521 show that the color of these moons becomes more similar to the rings the closer they are to Saturn.
522 This result suggests there is an ongoing accretion of a reddish chromophore that may be a mixture
523 of organics and iron, onto the surfaces of the moons. The difference in color between the moons
524 and their adjacent ring may be explained by the accretion of bright, icy particles or, more likely,
525 water vapor from the E-ring. In essence each moon's surface is subjected to a balance between
526 these two ongoing processes, with their distance from Saturn and Enceladus determining the final
527 result, as illustrated in Fig. 4F. The detection of abundant ice grains by CDA supports this view.
528 The bluer core of Atlas is also explained by the accretion of E-ring particles, which have a wider
529 range of inclinations than main ring particles. If the ring moons are made out of the same material
530 as the rings, they would of course have been the same color, and the color gradient may come
531 *solely* from contamination by the E-ring.

532 The finding by MIMI of a dearth of high-energy ions also lessens the competing alteration
533 processes caused by the bombardment of magnetospheric particles. The strong crystalline water
534 ice band at 1.65 μm also suggests the lack of importance of these processes. This "low energy"
535 environment also renders comparisons with the identity of the red chromophore on the trailing
536 hemispheres of main moons of Saturn, especially Dione and Rhea, problematical, as they dwell in
537 a region where alterations by ions is significant and would tend to darken and redden the surfaces
538 (57). Finally, the possible contamination of Saturn's rings by bright icy particles or water vapor
539 qualifies the argument that the observed brightness of the rings bespeaks a recent formation (58).

The moons record a complex geologic history with groove formation caused by tidal stresses and accretion of ring particles. The CDA finding of a porous surface further supports substantial accretion. Although the topography and surface slopes strongly suggest the equatorial ridges of Pan and Atlas are accreted from the rings and are not formed by normal surface transport, the variety of forms of ridges on these objects, and the minimal ridges on Daphnis, show that much remains to be understood about their formation and relation to the main rings. The high resolution images strongly suggest exposures of a solid substrate distinct from the mobile regolith that frequently covers essentially all of many small Solar System objects. These exposures may eventually help reveal systematic trends of both solid body history and structures for the whole of the Saturn satellite system.

Acknowledgements

This paper was funded by the *Cassini* Project. Part of this research was carried out at the Jet Propulsion Laboratory, California Institute of Technology under contract to the National Aeronautics and Space Administration. Other parts of this work were supported by the Deutsches Zentrum für Luft- und Raumfahrt (OH 1401 and 1503) and the Deutsche Forschungsgemeinschaft (Ho5720/1-1), and by the Italian Space Agency.

References

1. C. C. Porco, E. Baker, J. Barbara, K. Beurle, A. Brahic, J. A. Burns, S. Charnoz, N. Cooper, D. D. Dawson, A. D. Del Genio, T. Denk, L. Dones, U. Dyudina, M. W. Evans, B. Giese, K. Grazier, P. Helfenstein, A. P. Ingersoll, R. A. Jacobson, T. V. Johnson, A. McEwen, C. D. Murray, G. Neukum, W. M. Owen, J. Perry, T. Roatsch, J. Spitale, S. Squyres, P. Thomas, M.

562 Tiscareno, E. Turtle, A. R. Vasavada, J. Veverka, R. Wagner, R. West, *Cassini* imaging science:
563 Initial results on Saturn's rings and small satellites. *Science* **307**, 1237-1242 (2005).

564 2. M. R. Showalter, Visual detection of 1981S13, Saturn's eighteenth satellite, and its role in the
565 Encke gap. *Nature* **351**, 709-713 (1991).

566 3. B. A. Smith, L. Soderblom, R. F. Beebe, J. M. Boyce, G. Briggs, A. Bunker, S. A. Collins, C.
567 Hansen, T. V. Johnson, J. L. Mitchell, R. J. Terrile, M. H. Carr, A. F. Cook, J. N. Cuzzi, J. B.
568 Pollack, G. E. Danielson, A. P. Ingersoll, M. E. Davies, G. E. Hunt, H. Masursky, E. M.
569 Shoemaker, D. Morrison, T. Owen, C. Sagan, J. Veverka, R. Strom, V. E. Suomi, Encounter
570 with Saturn - Voyager 1 imaging science results. *Science* **212**, 163-191 (1981).

571 4. S. Charnoz, A. Brahic, P. C. Thomas, C. C. Porco, The equatorial ridges of Pan and Atlas:
572 Terminal accretionary ornaments? *Science* **318**, 1622-1624 (2007).

573 5. C. C. Porco, P. C. Thomas, J. W. Weiss, D. C. Richardson, Saturn's small inner satellites:
574 Clues to their origins. *Science* **318**, 1602 (2007).

575 6. P. C. Thomas, J. A. Burns, M. Hedman, P. Helfenstein, S. Morrison, M. S. Tiscareno, J.
576 Veverka, The inner small satellites of Saturn: A variety of worlds. *Icarus* **226**, 999-1019 (2013).

577 7. G. Filacchione, F. Capaccioni, R. N. Clark, J. N. Cuzzi, D. P. Cruikshank, A. Coradini, P.
578 Cerroni, P. D. Nicholson, T. B. McCord, R. H. Brown, B. J. Buratti, F. Tosi, R. M. Nelson, R.
579 Jaumann, K. Stephan, Saturn's icy satellites investigated by *Cassini*-VIMS. II. Results at the end
580 of nominal mission. *Icarus* **206**, 507-523 (2010).

581 8. G. Filacchione, F. Capaccioni, M. Ciarniello, R. N. Clark, J. N. Cuzzi, P. D. Nicholson, D. P.
582 Cruikshank, M. M. Hedman, B. J. Buratti, J. I. Lunine, L. A. Soderblom, F. Tosi, P. Cerroni, R.

583 H. Brown, T. B. McCord, R. Jaumann, K. Stephan, K. H. Baines, E. Flamini, Saturn's icy
584 satellites and rings investigated by *Cassini*-VIMS: III - Radial compositional variability. *Icarus*
585 **220**, 1064-1096 (2012).

586 9. G. Filacchione, F. Capaccioni, R. N. Clark, P. D. Nicholson, D. P. Cruikshank, J. N. Cuzzi, J.
587 I. Lunine, R. H. Brown, P. Cerroni, F. Tosi, M. Ciarniello, B. J. Buratti, M. M. Hedman, E.
588 Flamini, The radial distribution of water ice and chromophores across Saturn's system.
589 *Astrophys. J.* **766**, 76-80 (2013).

590 10. B. J. Buratti, J. M. Bauer, M. D. Hicks, J. A. Mosher, G. Filacchione, T. Momary, K. H.
591 Baines, R. H. Brown, R. N. Clark, P. D. Nicholson, *Cassini* spectra and photometry 0.25-5.1 μm
592 of the small inner satellites of Saturn. *Icarus* **206**, 524-536 (2010).

593 11. R. N. Clark, D. P. Cruikshank, R. Jaumann, R. H. Brown, K. Stephan, C. M. Dalle Ore, K. E.
594 Livo, N. Pearson, J. M. Curchin, T. M. Hoefen, B. J. Buratti, G. Filacchione, The surface
595 composition of Iapetus: Mapping results from *Cassini* VIMS. *Icarus* **218**, 831-860 (2012).

596 12. P. Schenk, D. P. Hamilton, R. E. Johnson, W. B. McKinnon, C. Paranicas, J. Schmidt, M. R.
597 Showalter, Plasma, plumes and rings: Saturn system dynamics as recorded in global color
598 patterns on its midsize icy satellites. *Icarus* **211**, 740-757 (2011).

599 13. A. R. Hendrix, G. Filacchione, C. Paranicas, P. Schenk, F. Scipioni, Icy Saturnian satellites:
600 Disk-integrated UV-IR characteristics and links to exogenic processes. *Icarus* **300**, 103-114
601 (2018).

602 14. T. V. Johnson, J. I. Lunine, Saturn's moon Phoebe as a captured body from the outer Solar
603 System. *Nature* **435**, 69-71 (2005).

604 15. C. C. Porco, R. A. West, S. Squyres, A. McEwen, P. Thomas, C. D. Murray, A. Del Genio,
605 A. P. Ingersoll, T. V. Johnson, G. Neukum, J. Veverka, L. Dones, A. Brahic, J. A. Burns, V.
606 Haemmerle, B. Knowles, D. Dawson, T. Roatsch, K. Beurle, W. Owen, *Cassini* maging science:
607 Instrument characteristics and anticipated scientific investigations at Saturn. *Space Sci. Revs.*
608 **115**, 363-497 (2004).

609 16. R. H. Brown, K. H. Baines, G. Bellucci, J.-P. Bibring, B. J. Buratti, F. Capaccioni, P.
610 Cerroni, R. N. Clark, A. Coradini, D. P. Cruikshank, P. Drossart, V. Formisano, R. Jaumann, Y.
611 Langevin, D. L. Matson, T. B. McCord, V. Mennella, E. Miller, R. M. Nelson, P. D. Nicholson,
612 B. Sicardy, C. Sotin, The *Cassini* Visual and Infrared Mapping Spectrometer (VIMS)
613 investigation. *Space Sci. Res.* **115**, 111-118 (2004).

614 17. F. M. Flasar, V. G. Kunde, M. M. Abbas, R. K. Achterberg, P. Ade, A. Barucci, B. Bézard,
615 G. L. Bjoraker, J. C. Brasunas, S. Calcutt, R. Carlson, C. J. Césarsky, B. J. Conrath, A. Coradini,
616 R. Courtin, A. Coustenis, S. Edberg, S. Edgington, C. Ferrari, T. Fouchet, D. Gautier, P. J.
617 Gierasch, K. Grossman, P. Irwin, D. E. Jennings, E. Lellouch, A. A. Mamoutkine, A. Marten, J.
618 P. Meyer, C. A. Nixon, G. S. Orton, T. C. Owen, J. C. Pearl, R. Prangé, F. Raulin, P. L. Read, P.
619 N. Romani, R. E. Samuelson, M. E. Segura, M. R. Showalter, A. A. Simon-Miller, M. D. Smith,
620 J. R. Spencer, L. J. Spilker, F. W. Taylor, Exploring the Saturn system in the thermal infrared:
621 The composite infrared spectrometer. *Space Sci. Res.* **115**, 169-297 (2004).

622 18. L. W. Esposito, C. A. Barth, J. E. Colwell, G. M. Lawrence, W. E. McClintock, A. I. F.
623 Stewart, H. U. Keller, A. Korth, H. Lauche, M. C. Festou, A. L. Lane, C. J. Hansen, J. N. Maki,
624 R. A. West, H. Jahn, R. Reulke, K. Warlich, D. E. Shemansky, Y. L. Yung, The *Cassini*
625 ultraviolet imaging spectrograph investigation. *Space Sci. Res.* **115** 299-361 (2004).

626 19. R. Srama, T. J. Ahrens, N. Altobelli, S. Auer, J. G. Bradley, M. Burton, V. V. Dikarev, T.
627 Economou, H. Fechtig, M. Görlich, M. Grande, A. Graps, E. Grün, O. Havnes, S. Helfert, M.
628 Horanyi, E. Igenbergs, E. K. Jessberger, T. V. Johnson, S. Kempf, A. V. Krivov, H. Krüger, A.
629 Mocker-Ahlreep, G. Moragas-Klostermeyer, P. Lamy, M. Landgraf, D. Linkert, G. Linkert, F.
630 Lura, J. A. M. McDonnell, D. Möhlmann, G. E. Morfill, M. Müller, M. Roy, G. Schäfer, G.
631 Schlotzhauer, G. H. Schwehm, F. Spahn, M. Stübig, J. Svestka, V. Tschernjawski, A. J.
632 Tuzzolino, R. Wäsch, H. A. Zook, The *Cassini* cosmic dust analyzer. *Space Sci. Res.* **114**, 465-
633 518 (2004).

634 20. S. M. Krimigis, D. G. Mitchell, D. C. Hamilton, S. Livi, J. Dandouras, S. Jaskulek, T. P.
635 Armstrong, J. D. Boldt, A. F. Cheng, G. Gloeckler, J. R. Hayes, K. C. Hsieh, W.-H. Ip, E. P.
636 Keath, E. Kirsch, N. Krupp, L. J. Lanzerotti, R. Lundgren, B. H. Mauk, R. W. McEntire, E. C.
637 Roelof, C. E. Schlemm, B. E. Tossman, B. Wilken, D. J. Williams, Magnetosphere IMaging
638 Instrument (MIMI) on the *Cassini* mission to Saturn/Titan. *Space Sci. Res.* **114**, 233-329 (2004).

639 21. M. M. Hedman, C. D. Murray, N. J. Cooper, M. S. Tiscareno, K. Beurle, M. W. Evans, J. A.
640 Burns, Three tenuous rings/arcs for three tiny moons. *Icarus* **199**, 378-386 (2009).

641 22. M. M. Hedman, N. J. Cooper, C. D. Murray, K. Beurle, M. W. Evans, M. S. Tiscareno, J. A.
642 Burns, Aegaeon (Saturn LIII), a G-ring object. *Icarus* **207**, 433-446 (2010).

643 23. S. J. Morrison, P. C. Thomas, M. S. Tiscareno, J. A. Burns, J. Veverka, Grooves on small
644 Saturnian satellites and other objects: Characteristics and significance. *Icarus* **204**, 262-270
645 (2009).

646 24. M. S. Tiscareno, P. C. Thomas, J. A. Burns, The rotation of Janus and Epimetheus. *Icarus*
647 **204**, 254-261 (2009).

648 25. N. J. Cooper, S. Renner, C. D. Murray, M. W. Evans, Saturn's inner satellites: Orbits,
649 masses, and the chaotic motion of Atlas from new *Cassini* imaging observations. *Astron. J.* **149**,
650 27-45 (2015).

651 26. J. W. Weiss, C. C. Porco, M. S. Tiscareno, Ring edge waves and the masses of nearby
652 satellites. *Astron. J.* **138**, 272-286 (2009).

653 27. S. J. Ostro, J.-L. Margot, L. A. M. Benner, J. D. Giorgini, D. J. Scheeres, E. G. Fahnestock,
654 S. B. Broschart, J. Bellerose, M. C. Nolan, C. Magri, P. Pravec, P. Scheirich, R. Rose, R. F.
655 Jurgens, E. M. De Jong, S. Suzuki, Radar imaging of binary near-Earth asteroid (66391) 1999
656 KW4. *Science* **314**, 1276-1280 (2006).

657 28. A. W. Harris, E. G. Fahnestock, P. Pravec, On the shapes and spins of “rubble pile”
658 asteroids. *Icarus* **199**, 310-318 (2009).

659 29. S. J. Weidenschilling, A possible origin for the grooves of PHOBOS. *Nature* **282**, 697
660 (1979).

661 30. D. L. Buczowski, O. S. Barnouin-Jha, L. M. Prockter, 433 Eros lineaments: Global mapping
662 and analysis. *Icarus* **193**, 39-52 (2008).

663 31. M. Nayak, E. Asphaug, Sesquinary catenae on the martian satellite Phobos from reaccrction
664 of escaping ejecta. *Nature Communications.* **7**, 12591 (2016).

665 32. West, B. Knowles, E. Birath, S. Charnoz, D. Di Nino, M. Hedman, P. Helfenstein, A.
666 McEwen, J. Perry, C. Porco, J. Salmon, H. Throop, D. Wilson, In-flight calibration of the
667 *Cassini* imaging science sub-system cameras. *Planet. and Space Sci.* **58**, 1475-1488 (2010).

668 33. P. C. Thomas, M. Tiscareno, P. Helfenstein, "The Inner Small Satellites of Saturn and
 669 Hyperion." in *Enceladus and the Icy Moons of Saturn*, P. Schenk, R. Clark, C. Howett, A.
 670 Verbiscer, H. Waite, Eds. (University of Arizona, 2018).

671 34. R. M. E. Mastrapa, R. H. Brown, Ion irradiation of crystalline H₂O-ice: Effect on the 1.65-
 672 μ m band. *Icarus* **183**, 207-214 (2006).

673 35. R. N. Clark, Water frost and ice - The near-infrared spectral reflectance 0.65-2.5 microns. *J*
 674 *Geophys. Res.* **86**, 3087-3096 (1981).

675 36. D. P. Hamilton, J. A. Burns, Origin of Saturn's E-ring: Self-sustained, naturally. *Science* **264**,
 676 550-553 (1994).

677 37. B. J. Buratti, J. A. Mosher, T. V. Johnson, Albedo and color maps of the Saturnian satellites.
 678 *Icarus* **87**, 339-357 (1990).

679 38. A. Verbiscer, R. French, M. Showalter, P. Helfenstein, Enceladus: Cosmic graffiti artist
 680 caught in the act. *Science* **315**, 815 (2007).

681 39. C. C. Porco, Rings of Saturn (R/2006 S 1, R/2006 S 2, R/2006 S 3, R/2006 S 4). *IAU Circ.*,
 682 No. 8759, #1 (2006).

683 40. A. V. Krivov, M. Sremečvić, F. Spahn, V. V. Dikarev, K. V. Kholshchevnikov, Impact-
 684 generated dust clouds around planetary satellites: spherically symmetric case. *Planetary and*
 685 *Space Science* **51**, 251-269 (2003).

686 41. F. Spahn, N. Albers, M. Hörning, S. Kempf, A. V. Krivov, M. Makuch, J. Schmidt, M. Seiß,
 687 S. Miodrag, E-ring dust sources: Implications from *Cassini*'s dust measurements. *Planet. and*
 688 *Space Science* **54**, 1024-1032 (2006).

689 42. S. Kempf, N. Altobelli, J. N. Cuzzi, P. R. Estrada, R. Srama, submitted to Nature (2018).

690 43. H. Krüger, A. V. Krivov, M. Sremčević, E. Grün, Impact-generated dust clouds surrounding
691 the Galilean moons. *Icarus* **164**, 170-187 (2003).

692 44. J. A. van Allen, B. A. Randall, D. N. Baker, C. K. Goertz, D. D. Sentman, M. F. Thomsen,
693 H. R. Flindt, Pioneer 11 observations of energetic particles in the Jovian magnetosphere. *Science*
694 **188**, 459-462 (1975).

695 45. F. B. McDonald, A. W. Schardt, J. H. Trainor, If you've seen one magnetosphere, you haven't
696 seen them all - Energetic particle observations in the Saturn magnetosphere. *J. Geophys. Res.* **85**,
697 5813-5830 (1980).

698 46. S. M. Krimigis, D. G. Mitchell, D. C. Hamilton, N. Krupp, S. Livi, E. C. Roelof, J.
699 Dandouras, T. P. Armstrong, B. H. Mauk, C. Paranicas, P. C. Brandt, S. Bolton, A. F. Cheng, T.
700 Choo, G. Gloeckler, J. Hayes, K. C. Hsieh, W.-H. Ip, S. Jaskulek, E. P. Keath, E. Kirsch, M.
701 Kusterer, A. Lagg, L. J. Lanzerotti, D. LaVallee, J. Manweiler, R. W. McEntire, W. Rasmuss,
702 Dynamics of Saturn's magnetosphere from MIMI during *Cassini*'s orbital insertion. *Science* **307**,
703 1270-1273 (2005).

704 47. E. Roussos, N. Krupp, P. Kollmann, C. Paranicas, D. G. Mitchell, S. M. Krimigis, M.
705 Andriopoulou, Evidence for dust-driven, radial plasma transport in Saturn's inner radiation belts.
706 *Icarus* **274**, 272-283 (2016).

707 48. J. A. van Allen, Findings on rings and inner satellites of Saturn of Pioneer 11. *Icarus* **51**,
708 509-527 (1982).

709 49. H. Cao, C. T. Russell, U. R. Christensen, M. K. Dougherty, M. E. Burton, Saturn's very
710 axisymmetric magnetic field: No detectable secular variation or tilt. *Earth and Planet. Sci. Lett.*
711 **304**, 22-28 (2011).

712 50. E. Roussos, N. Krupp, T. P. Armstrong, C. Paranicas, D. G. Mitchell, S. M. Krimigis, G. H.
713 Jones, K. Dialynas, N. Sergis, D. C. Hamilton, Discovery of a transient radiation belt at Saturn.
714 *Geophys. Res. Lett.* **35**, 22106 (2008).

715 51. P. Kollmann, E. Roussos, A. Kotova, C. Paranicas, N. Krupp, The evolution of Saturn's
716 radiation belts modulated by changes in radial diffusion. *Nature Astronomy*. **1**, 872-877 (2017).

717 52. B. D. Teolis, G. H. Jones, P. F. Miles, R. L. Tokar, B. A. Magee, J. H. Waite, E. Roussos, D.
718 T. Young, F. J. Crary, A. J. Coates, R. E. Johnson, W.-L. Tseng, R. A. Baragiola, *Cassini* finds
719 an oxygen-carbon dioxide atmosphere at Saturn's icy moon Rhea. *Science* **330**, 1813 (2010).

720 53. P. Kollmann, E. Roussos, C. Paranicas, N. Krupp, C. M. Jackman, E. Kirsch, K.-H.
721 Glassmeier, Energetic particle phase space densities at Saturn: *Cassini* observations and
722 interpretations. *J. Geophys. Res. (Space Physics)* **116**, A05222 (2011).

723 54. C. Paranicas, E. Roussos, N. Krupp, P. Kollmann, A. R. Hendrix, T. Cassidy, R. E. Johnson,
724 P. Schenk, G. Jones, J. Carbary, D. G. Mitchell, K. Dialynas, Energetic charged particle
725 weathering of Saturn's inner satellites. *Planet. Space Sci.* **61**, 60-65 (2012).

726 55. B. H. Mauk, D. G. Mitchell, R. W. McEntire, C. P. Paranicas, E. C. Roelof, D. J. Williams,
727 S. M. Krimigis, A. Lagg, Energetic ion characteristics and neutral gas interactions in Jupiter's
728 magnetosphere. *Journal Geophys. Res. (Space Physics)* **109**, A09S12 (2004).

729 56. J. F. Cooper, R. E. Johnson, B. H. Mauk, H. B. Garrett, N. Gehrels, Energetic Ion and
730 Electron Irradiation of the Icy Galilean Satellites. *Icarus* **149**, 133-159 (2001).

731 57. E. Roussos, N. Krupp, C. Paranicas, J. F. Carbary, P. Kollmann, S. M. Krimigis, D. G.
732 Mitchell, The variable extension of Saturn's electron radiation belts. *Planet. Space Sci.* **104**, 3-17
733 (2014).

734 58. J. N. Cuzzi, J. A. Burns, Charged particle depletion surrounding Saturn's F ring - Evidence
735 for a moonlet belt? *Icarus* **74**, 284-324 (1988).

736 59. R. E. Johnson, T. I. Quickenden, Photolysis and radiolysis of water ice on outer solar system
737 bodies. *J. Geophys. Res.* **102**, 10985-10996 (1997).

738 60. Z. Zhang, A. G. Hayes, M. A. Janssen, P. D. Nicholson, J. N. Cuzzi, I. de Pater, D. E. Dunn,
739 Exposure age of Saturn's A and B rings, and the *Cassini* Division as suggested by their non-icy
740 material content. *Icarus* **294**, 14-42 (2017).

741

742 **Table 1: Summary of five “best ever” flybys of Saturn’s ring moons during the Ring-**
743 **grazing Orbits**

744

| Moon | Semi-major axis (R_s) | Rotation rate (days) | Date of flyby | Closest approach (km) | Spatial resolution improvement factor | Best resolution (Imaging; m/pixel) |
|---------|---------------------------|----------------------|---------------|-----------------------|---------------------------------------|------------------------------------|
| Pan | 2.22 | 0.575 | 7 March 2017 | 22,247 | 2 | 147 |
| Daphnis | 2.26 | 0.594 | 16 Jan 2017 | 22,336 | >10 | 170 |
| Atlas | 2.29 | 0.602 | 12 April 2017 | 10,848 | 2 | 76 |
| Pandora | 2.35 | 0.629 | 18 Dec 2016 | 22,157 | ~3 | 132 |

| | | | | | | |
|------------|------|-------|-------------|--------------|---|----|
| Epimetheus | 2.51 | 0.695 | 30 Jan 2017 | 3,625 | 6 | 36 |
|------------|------|-------|-------------|--------------|---|----|

Table 2: Sizes and mean densities of Saturn’s ring moons described in this paper and Janus

| Object | a, km | b, km | c, km | R _m , km | Density, kgm ⁻³ | Gravity, cms ⁻² |
|------------|-----------|----------|----------|---------------------|----------------------------|----------------------------|
| Pan | 17.3±0.2 | 14.1±0.2 | 10.5±0.7 | 13.7±0.3 | 400±32 | 0.2-1.7 |
| Daphnis | 4.9±0.3 | 4.2±0.8 | 2.8±0.6 | 3.9±0.5 | 274±142 | 0.0-0.4 |
| Atlas | 20.4±0.1 | 17.7±0.2 | 9.3±0.3 | 14.9±0.2 | 412±19 | 0.0-1.7 |
| Pandora | 51.5±0.3 | 39.5±0.3 | 31.5±0.2 | 40.0±0.3 | 509±12 | 2.0-5.9 |
| Epimetheus | 64.8±0.4 | 58.1±0.8 | 53.5±0.4 | 58.6±0.5 | 625±16 | 6.6-10.9 |
| Janus | 101.8±0.9 | 93.0±0.3 | 74.5±0.3 | 89.0±0.5 | 642±10 | 642±10 |

Semi-axes are of ellipsoids fit to shape models and rescaled to volume of the model. R_m, the mean radius, is the radius of a sphere of equivalent volume.

Masses for Atlas, Pandora and Epimetheus are from (25). Masses of Pan and Daphnis are from (26). For a full table of Saturn’s small inner moons see (supplementary materials).

Supplementary Materials

Overview of the Ring and Moon System of Saturn
Complete Table of Densities
Methods: Visible Infrared Mapping Spectrometer
Methods: CIRS
Methods:CDA

Overview of the Ring and Moon System of Saturn

Saturn has 62 moons that group into several categories. Besides the five main inner moons (Mimas, Enceladus, Tethys, Dione, and Rhea), Hyperion, Titan, and Iapetus, the outer irregular moons, which include Phoebe, the planet has a family of ring moons that orbit in gaps within Saturn’s rings (Pan in the Encke gap and Daphnis in the Keeler gap) or skirt the outer edge of the A-ring (Atlas) and the F-ring (Prometheus and Pandora). The coorbital moons Janus and Epimetheus, which exchange an orbit outside the A-ring approximately every four years, are often classified as ring moons as well. Figure 1S illustrates the position of the ring moons within Saturn’s ring system.

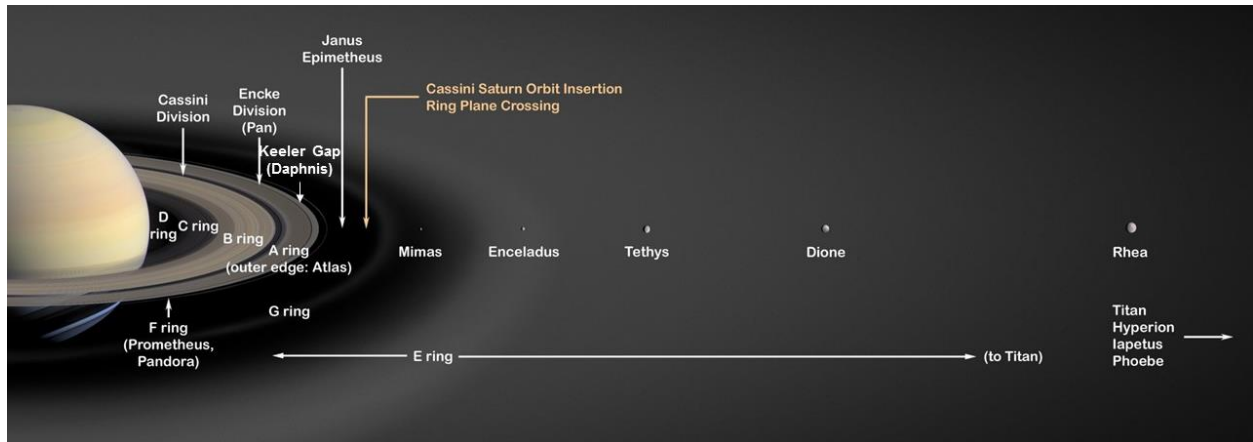


Figure 1S. A diagram showing the location of the main ring system of Saturn, the main inner moons, and the ring moons Pan, Daphnis, Atlas, Pandora, and Prometheus. The coorbital moons Janus and Epimetheus are often regarded as ring moons as well. Based on NASA PIA

Table S1: Sizes and mean densities of small Saturnian satellites

| Object | a, km | b, km | c, km | Rm, km | density, kgm^{-3} | gravity, cms^{-2} |
|------------|-----------------|----------------|----------------|----------------|----------------------------|----------------------------|
| Pan | 17.3 ± 0.2 | 14.1 ± 0.2 | 10.5 ± 0.7 | 13.7 ± 0.3 | 400 ± 32 | $0.2 - 1.7$ |
| Daphnis | 4.9 ± 0.3 | 4.2 ± 0.8 | 2.8 ± 0.6 | 3.9 ± 0.5 | 274 ± 142 | $0.0 - 0.4$ |
| Atlas | 20.4 ± 0.1 | 17.7 ± 0.2 | 9.3 ± 0.3 | 14.9 ± 0.2 | 412 ± 19 | $0.0 - 1.7$ |
| Prometheus | 68.5 ± 0.5 | 40.5 ± 1.4 | 28.1 ± 0.4 | 42.8 ± 0.7 | 460 ± 21 | $0.8 - 5.8$ |
| Pandora | 51.5 ± 0.3 | 39.5 ± 0.3 | 31.5 ± 0.2 | 40.0 ± 0.3 | 509 ± 12 | $2.0 - 5.9$ |
| Epimetheus | 64.8 ± 0.4 | 58.1 ± 0.8 | 53.5 ± 0.4 | 58.6 ± 0.5 | 625 ± 16 | $6.6 - 10.9$ |
| Janus | 101.8 ± 0.9 | 93.0 ± 0.3 | 74.5 ± 0.3 | 89.0 ± 0.5 | 642 ± 10 | $10.9 - 16.9$ |
| Aegaeon | 0.7 ± 0.0 | 0.3 ± 0.1 | 0.2 ± 0.0 | 0.3 ± 0.0 | 539 ± 140 | $0.001 - 0.005$ |
| Methone | 1.9 ± 0.0 | 1.3 ± 0.0 | 1.2 ± 0.0 | 1.4 ± 0.0 | 307 ± 30 | $0.1 - 0.1$ |
| Pallene | 2.9 ± 0.4 | 2.1 ± 0.3 | 1.8 ± 0.3 | 2.2 ± 0.3 | 251 ± 75 | $0.1 - 0.2$ |
| Telesto | 16.6 ± 0.3 | 11.7 ± 0.3 | 9.6 ± 0.2 | 12.3 ± 0.3 | | |
| Calypso | 14.7 ± 0.3 | 9.3 ± 0.9 | 6.4 ± 0.3 | 9.5 ± 0.4 | | |
| Polydeuces | 1.5 ± 0.3 | 1.3 ± 0.4 | 1.0 ± 0.2 | 1.3 ± 0.3 | | |
| Helene | 22.6 ± 0.2 | 19.6 ± 0.3 | 13.3 ± 0.2 | 18.1 ± 0.2 | | |

Semi-axes are of ellipsoids fit to shape models and rescaled to volume of the model. Rm, mean radius, is the radius of a sphere of equivalent volume.

Masses for Janus, Epimetheus, Atlas, Prometheus, and Pandora are from (25). Masses of Pan and Daphnis from (26). Masses of Aegaeon, Pallene, Methone are estimates from equilibrium shape interpretations (6). Masses of Telesto, Calypso, Polydeuces and Helene are unknown.

Methods: Visible Infrared Mapping Spectrometer Observations

The wavelength range of VIMS, from 0.35 μm to 5.1 μm , covers 99% of the reflected solar spectrum in 352 spectral channels, with spatial resolution of 0.5 mradian and spectral resolution ranging from 1.46 nm in the visible region (0.35-1.05 μm) to 16.6 nm in the NIR (0.85-5.1 μm). These are key spectral ranges for identifying volatiles including water ice, organics, and minerals. VIMS was also capable of a high-resolution spatial mode offering double resolution in one dimension. The instrument had separate visible and infrared channels, with visible light captured by a 512X512 CCD detector and IR photons captured on a 1X256 InSb detector.

Fig. 4 shows the best images for the five moons at 1.38 (1.48 for Pan), 2.01, and 3.50 μm (only 2.01 is shown for Daphnis, due to the low spatial resolution of the images; a positive identification was made by coaligning the VIMS and ISS images). A ratio image of 1.76/2.01 μm , representing the spectral continuum to the most prominent water ice band, is also shown. No spatial variations in the water icy band imply uniformity in abundance and texture on the individual moons. Due to its much higher spatial resolution, ISS is better suited to seeking visible color variations on the moons.

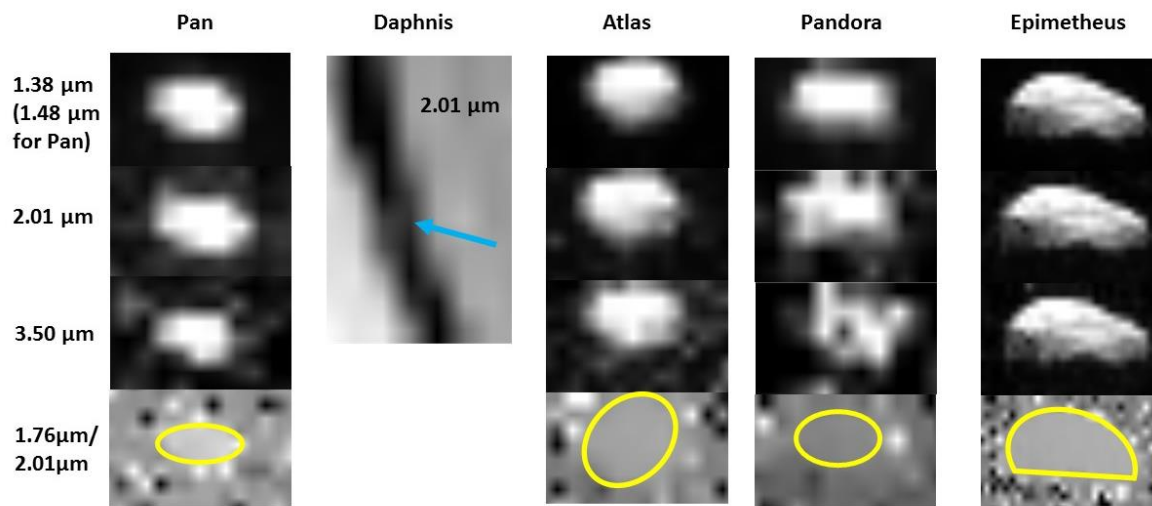


Fig. 2S. Infrared images of the five ring moons studied during the Ring-grazing Orbits at 1.38 (1.48 for Pan), 2.01 and 3.50 μm . The bottom row is a ratio of the continuum at 1.76 μm to the water ice absorption band at 2.01 μm , showing uniformity on all the moons' surfaces (the images for Daphnis were too noisy to construct this ratio).

Methods: The Cassini Infrared Spectrometer

The detections of both Atlas and Epimetheus were made using dedicated CIRS scans bracketed by ISS observations. Epimetheus was detected on 30 Jan 2017 during a scan that occurred between 19:54:20 to 20:05:50 UTC, at a distance that decreased from 80,179 to 67,237 km. During this time the sub-

spacecraft position changed from 345.0° W/73.5° N to 346.5° W/73.7° N, the local time at the sub-spacecraft point increased from 271° to 276° and the phase increased slightly from 68.0° to 68.5°.

Atlas was detected a few months later, on 12 April 2017, during a scan that ran from 13:16:39 to 13:24:40 UTC, at a distance that decreased from 33,572 km to 24,580 km. During that time the phase at the sub-spacecraft point decreased from 51.2° to 47.2°, the sub-spacecraft position changed from 141.9° W/60.1° N to 149.8° W/52.1° N, and the local time at the sub-spacecraft point decreased from 226° to 221°.

In both detections CIRS used its focal plane 3 (FP3, which covers 570–1125 cm⁻¹) to scan the target and background sky. The images have been rotated so they are also in RA/Dec coordinates. However, the scale of the CIRS data and the ISS images is notably different, as indicated by the 10 km scale bar given in Fig. 5 in the main text. Images of Atlas taken before and after the CIRS scan were ISS image N00279648 using CL1 and CL2 filters on Apr. 12, 2017 at 1:15 UT; ISS image N00279649 taken using CL1 and CL2 filters on Apr. 12, 2017 1:27 UT. Images of Epimetheus taken before and after the CIRS scan were ISS image N00275708 taken using CL1 and CL2 filters on Jan. 30, 2017 7:53 UT and ISS image N00275709 taken using CL1 and UV3 filters on Jan. 30, 2017 8:07 UT.

Numerical simulations and the lifetimes of the dust particles

We performed numerical simulations of dust particles in the Janus-Epimetheus ring to estimate their lifetimes. In Fig. 1, the solid line shows the fraction of remaining particles (those which did not yet collide with Janus, Epimetheus, Saturn or its dense rings). To obtain the mean lifetime τ of the dust particles, we fit an exponential function $f(t) = \exp(-t/\tau)$ to the simulation results, shown as dashed line, yielding $\tau = 60$ years.

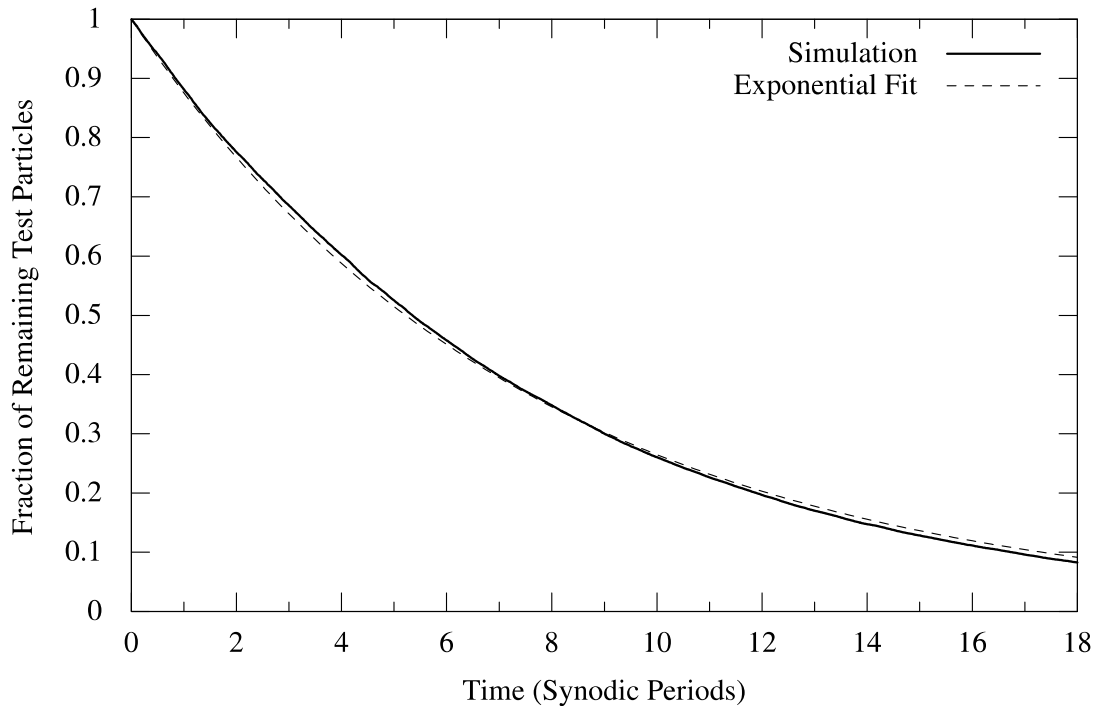


Fig 3S. Particle Lifetimes. The solid line shows the evolution of the fraction of remaining particles (which did not collide with Janus, Epimetheus, Saturn or its dense rings), whereas the dashed line denotes an exponential fit to this evolution leading to a mean lifetime of $\tau = 60$ years. The synodic period of Janus and Epimetheus is about 8 years.

We assume the dust particles to be spheres with a radius of $s = 1.6 \mu\text{m}$, which is consistent with the size of particles measured to comprise the Janus-Epimetheus ring by the HRD detector of Cassini's CDA. In the simulations, we consider the gravity of Saturn (including its oblateness up to 6th order), the gravity of Janus and Epimetheus, as well as solar radiation pressure and the Lorentz force due to Saturn's magnetic field (considered as a dipole field). Table 1 summarizes the parameters used in the simulations.

We integrated the equations of motion of 40,000 particles for about 150 years. For simplicity, the initial eccentricities and inclinations of the dust particles were chosen to be Rayleigh distributed with mean values of $\langle e \rangle = 0.0068$ and $\langle i \rangle = 0.17$ deg, resembling a ring width of about 2000 km and a ring scale height of 350 km. The initial ephemeris data of the Sun, Janus, and Epimetheus were obtained from data provided by the NAIF SPICE toolkit using the kernel files de430.bsp, sat375.bsp, sat378.bsp, and cpck23Aug2007.tpc.

Table 1. Parameters used in the simulations: solar radiation pressure efficiency factor Q_{pr} , solar constant Q_s , electrostatic grain potential ϕ_{grain} , dipole term of Saturn's magnetic field g_{10} , and the gravitational harmonic coefficient J_2 , J_4 , and J_6 .

| Parameter | Value | Reference |
|-----------------------------|------------------------------------|------------------|
| <i>Radiation Pressure:</i> | | |
| Q_{pr} | 0.49 | (Liu, 2016) |
| Q_s | $1.36 \times 10^3 \text{ Wm}^{-2}$ | |
| <i>Lorentz Force:</i> | | |
| ϕ_{grain} | -1.6 V | (Horanyi, 2009) |
| g_{10} | $2.1162 \times 10^{-5} \text{ T}$ | (Burton, 2009) |
| <i>Saturn's Oblateness:</i> | | |
| J_2 | 1.629071×10^{-2} | (Jacobson, 2006) |
| J_4 | -9.3583×10^{-4} | (Jacobson, 2006) |
| J_6 | 8.614×10^{-5} | (Jacobson, 2006) |

The lifetime of the particles in the Janus and Epimetheus ring is also restricted by the surrounding plasma, neglected in our simulations. The permanent bombardment of the dust particles by Saturn's plasma particles leads to a sputtering of their surface, which reduces the size of the particles. The typical plasma sputtering rate in the E ring is about $1 \mu\text{m}$ in 50 years (Jurac, 2001). However, the plasma density

is decreasing by two orders of magnitude towards Saturn (Elrod, 2014) which increases the sputtering lifetime of a $1.6 \mu\text{m}$ sized particle to $\tau_{\text{sputt}} = 8000$ years.

Collisions with the plasma particles further accelerate the dust particles causing an outward drift (plasma drag). While drift rates of 1000 km/yr are typical in the E ring for $1.6 \mu\text{m}$ sized grains (Horanyi, 2008), the drift rate in the Janus-Epimetheus region is only 10 km/yr due to the lower plasma densities (Elrod, 2014). Therefore, a dust particle is estimated to leave the Janus-Epimetheus ring after about 210 years, assuming a HWHM of 2100 km .

Summarizing, the collisions with the moons are the dominating sink for the ring particles leading to a typical lifetime of about 60 years, which provides a fair explanation of the impact-generated ring embracing the orbits of Janus and Epimetheus.

Impact-ejection model

It is assumed that the dust in the Janus-Epimetheus ring is generated by the process of impact-ejection – the ejection of secondary dust particles by impacts of fast micro-meteoroids onto atmosphereless planetary satellites.

In order to estimate the dust densities in the ring, we apply the impact-ejection model (Krivov, 2003). In this model, the total mass ejected from the target surface per unit time is given by

$$M^+ = F_{\text{imp}} Y S, \quad (1)$$

where F_{imp} is the impactor mass flux (density) at the target and S is the target's cross sectional area (Krivov, 2003). Y is the yield defined as the ratio of the total mass ejected by an impactor to its mass, which strongly depends on the impact speed v_{imp} as well as the impactor mass m_{imp} and the composition of the target surface. We use an empirical relation for the yield (Koschny, 2001), which reads (in SI units)

$$Y = 2.85 \times 10^{-8} (0.015)^{\frac{x}{100}} \rho_{\text{ice}}^{0.23} m_{\text{imp}}^{0.23} v_{\text{imp}}^{2.46}, \quad (2)$$

where $\rho_{\text{ice}} \approx 930 \text{ kg/m}^3$ is the mass density of ice at a temperature of 100 K .

The impactor flux is $2.7 \times 10^{-16} \text{ kg m}^{-2} \text{ s}^{-1} \leq F_{\text{imp}}^{\infty} \leq 3.3 \times 10^{-15} \text{ kg m}^{-2} \text{ s}^{-1}$ at the Hill radius of Saturn and has been obtained together with the impactor size and speed distributions from *in situ* measurements of the Cassini CDA (Kempf, 2018). The impactor flux and impact speeds are amplified due to gravitational focusing by the planet (Colombo, 1966; Spahn, 2006). At the planetocentric distance of Janus and Epimetheus ($2.5 R_s$), the mean focusing factors are ~ 4 for the impact speeds and ~ 25 for the impactor flux, and the mean yield is $Y \sim 3800$, averaged over the impact speeds and impactor sizes, respectively.

For the lower limit of the impactor flux, this gives a mass production rate of 0.64 kg/s for Janus and 0.27 kg/s for Epimetheus.

The cumulative size distribution of the debris is assumed to be a power law with exponent $-\alpha$, so that the number of particles with radii larger than s ejected from the target surface per unit time is given by

$$N^+(\geq s) = \frac{3 - \alpha}{\alpha} \frac{M^+}{m_{\max}} \left(\frac{s_{\max}}{s} \right)^\alpha, \quad (3)$$

where m_{\max} (s_{\max}) is the maximal ejecta mass (size). The index α depends on the target material and ranges from 1.5 for loose to 3 for solid targets (Krivov, 1998). *In situ* measurements give for the index of the size distribution values of $\alpha \sim 2.4$ for the dust atmospheres around the Galilean moons (Krüger, 2003), and a value of $\alpha \sim 2.7$ for the lunar dust atmosphere (Horanyi, 2015). The largest ejecta is typically similar in size to the largest impactor (Sachse, 2017).

For $\alpha = 2.4$ and $m_{\max} = 10^{-8}$ kg (an icy particle with $s_{\max} \approx 140$ μm), 6.9×10^{12} particles larger than 1.6 μm from Janus and 2.9×10^{11} from Epimetheus are ejected.

Impact experiments and scaling laws (Housen, 2011) show that the differential speed distribution is proportional to a power law with exponent $-\gamma - 1$

$$f(u) = \frac{\gamma}{u_{\min}^{-\gamma} - u_{\max}^{-\gamma}} u^{-\gamma-1} \Theta(u - u_{\min}) \Theta(u_{\max} - u), \quad (4)$$

where $\Theta(x)$ denotes the unit step function, which is one for $x \geq 0$ and zero otherwise. The index γ depends on properties of the target material and ranges from $\gamma = 1$ for highly porous to $\gamma = 2$ for nonporous materials (Krivov, 2003).

The minimal ejection speed u_{\min} is chosen so that the kinetic energy of the ejecta is a few (tens of) percent of the kinetic energy of the impactor (Asada, 1985; Hartmann, 1985). Hard surfaces (e.g. ice) are generally less dissipative than soft surfaces (e.g. snow, regolith). In case the ejecta sizes and ejection speeds are uncorrelated, the relation between Y , γ , and u_{\min} reads (Krüger, 2000)

$$\frac{K_e}{K_{\text{imp}}} = Y \frac{\gamma}{2 - \gamma} \left(\frac{u_{\min}}{v_{\text{imp}}} \right)^2 \left[\left(\frac{u_{\min}}{u_{\max}} \right)^{\gamma-2} - 1 \right] \quad \text{for } \gamma \neq 2 \quad (5)$$

and

$$\frac{K_e}{K_{\text{imp}}} = 2Y \left(\frac{u_{\min}}{v_{\text{imp}}} \right)^2 \ln \left(\frac{u_{\max}}{u_{\min}} \right) \quad \text{for } \gamma = 2, \quad (6)$$

where the subscripts “imp” and “e” refer to impactor and ejecta related variables, respectively.

The maximal ejection speed is larger than the escape velocity of the largest satellites in the Solar System ($u_{\max} > 3$ km/s). For example, impact-ejecta escape the gravity of the Galilean moons and form a dust ring between their orbits (Krivov, 2002). Integrating Equation (4) for speeds larger than the escape velocity, $u > v_{\text{esc}}$, gives the fraction of escaping ejecta.

Table 2S summarizes the parameters used for the impact-ejection model and the results.

| Parameter | Value | Reference/Comment |
|---------------------------|--|------------------------------|
| F_{imp}^{∞} | $2.7 \times 10^{-16} \text{ kg m}^{-2} \text{ s}^{-1}$ | (Kempf, 2018) |
| F_{imp} | $6.7 \times 10^{-15} \text{ kg m}^{-2} \text{ s}^{-1}$ | |
| Y | 3800 | |
| M^+ | 0.9 kg s^{-1} | 70% Janus and 30% Epimetheus |
| α | 2.4 | (Krüger, 2003) |
| m_{\max} | $1.0 \times 10^{-8} \text{ kg}$ | (Krivov, 2003) |
| $N^+(> s)$ | $9.8 \times 10^{11} \text{ s}^{-1}$ | 70% Janus and 30% Epimetheus |
| K_e/K_{imp} | 0.05 | |
| γ | 1.0 | (Krivov, 2003) |
| $N_{\text{esc}}^+(> s)$ | $5.5 \times 10^{10} \text{ s}^{-1}$ | 60% Janus and 40% Epimetheus |

Table 2. Parameters and results of the impact-ejection model.

References

- (1) S. Jurac, R. E. Johnson, J. D. Richardson, *Icarus* **149**, 384 (2001).
- (2) M. K. Elrod, W.-L. Tseng, A. K. Woodson, R. E. Johnson, *Icarus* **242**, 130 (2014).
- (3) M. Horányi, A. Juhász, G. E. Morfill, *Geophysical Research Letters* **35**, L04203 (2008).
- (4) X. Liu, M. Sachse, F. Spahn, J. Schmidt, *Journal of Geophysical Research (Planets)* **121**, 1141 (2016).
- (5) M. Horányi, J. A. Burns, M. M. Hedman, G. H. Jones, S. Kempf, *Saturn from Cassini-Huygens*, M. K. Dougherty, L. W. Esposito, S. M. Krimigis, eds. (2009), p. 511.
- (6) M. E. Burton, M. K. Dougherty, C. T. Russell, *Planetary and Space Science* **57**, 1706 (2009).
- (7) R. A. Jacobson, et al., *Astronomical Journal* **132**, 2520 (2006).
- (8) A. V. Krivov, M. Sremčević, F. Spahn, V. V. Dikarev, K. V. Kholshchevnikov, *Planetary and Space Science* **51**, 251 (2003).
- (9) D. Koschny, E. Grün, *Icarus* **154**, 402 (2001).

- 953 (10) S. Kempf, N. Altobelli, J. N. Cuzzi, P. R. Estrada, R. Srama, *submitted to Nature* (2018).
- 954 (11) G. Colombo, D. A. Lautman, I. I. Shapiro, *Journal of Geophysical Research* **71**, 5705 (1966).
- 955 (12) F. Spahn, et al., *Planetary and Space Science* **54**, 1024 (2006).
- 956 (13) A. Krivov, A. Jurewicz, *Planetary and Space Science* **47**, 45 (1998).
- 957 (14) H. Krüger, A. V. Krivov, M. Sremčević, E. Grün, *Icarus* **164**, 170 (2003).
- 958 (15) M. Horányi, et al., *Nature* **522**, 324 (2015).
- 959 (16) M. Sachse, *Icarus* **303**, 166 (2018).
- 960 (17) K. R. Housen, K. A. Holsapple, *Icarus* **211**, 856 (2011).
- 961 (18) N. Asada, *Journal of Geophysical Research* **90**, 12445 (1985).
- 962 (19) W. K. Hartmann, *Icarus* **63**, 69 (1985).
- 963 (20) H. Krüger, A. V. Krivov, E. Grün, *Planetary and Space Science* **48**, 1457 (2000).
- 964 (21) A. V. Krivov, H. Krüger, E. Grün, K.-U. Thiessenhusen, D. P. Hamilton, *Journal of Geophysical*
965 *Research (Planets)* **107**, 5002 (2002).
- 966
- 967
- 968